



Title	Surface velocities and ice-front positions of eight major glaciers in the Southern Patagonian Ice Field, South America, from 2002 to 2011
Author(s)	Muto, minami; Furuya, Masato
Citation	Remote sensing of environment, 139, 50-59 https://doi.org/10.1016/j.rse.2013.07.034
Issue Date	2013-12
Doc URL	http://hdl.handle.net/2115/54777
Type	article (author version)
File Information	furuya.pdf



[Instructions for use](#)

Surface Velocities and Ice-Front Positions of Eight Major Glaciers in the Southern Patagonian Ice Field, South America, from 2002 to 2011

Minami Muto and Masato Furuya

Department of Natural History Sciences, Graduate School of Science, Hokkaido University, N10W8, Kita-ku, Sapporo 060-0810, JAPAN.

Abstract

The Patagonian Ice Fields are known to have undergone rapid retreat of frontal positions and significant thinning of its glaciers over the past decades. However, surface velocities have been measured at only a few of these glaciers. Thus, it remains uncertain if and to what extent the glacier dynamics have changed over time and contributed to ice loss in these ice fields. In this study, we examine the temporal evolution of flow velocities and ice-front positions at eight major glaciers in the Southern Patagonian Ice Field (SPI; Hielo Patagónico Sur) by using Advanced Synthetic Aperture Radar (ASAR) images from the Environmental Satellite (Envisat) launched in 2002 by the European Space Agency and Advanced Land Observation Satellite/Phased Array-type L-band Synthetic Aperture Radar (ALOS/PALSAR) data recorded from 2002 to 2011. The examined eight glaciers include Glaciar Jorge Montt, Occidental, Pio XI (or Brügger), O'Higgins, Viedma, Upsala, Perito Moreno, and Grey. Not all the glaciers revealed significant changes in frontal positions and flow velocities in the study period. We detected significant temporal velocity changes at Glaciar Upsala, Jorge Montt, Occidental, and Pio XI.

Among these four glaciers, Glaciars Upsala, Jorge Montt, and Occidental revealed significant acceleration and terminus retreat and were undergoing dynamic–thinning. The markedly different absolute velocities but equally large longitudinal near-terminus stretching at the three glaciers support a calving model based on crevasse–depth criteria, which predict a calving position where crevasse–depths are equal to ice thickness; crevasse–depths are controlled by the longitudinal stretching rate. Meanwhile, Glaciar Pio XI revealed complex spatial and temporal evolution in surface velocities without significant retreat, and its dynamics remain enigmatic.

Keywords: glacier velocity, Southern Patagonia, calving glacier, synthetic aperture radar

1. Introduction

2 The Southern Patagonian Ice Field (SPI; Hielo Patagónico Sur) contains
3 the largest temperate glaciers in southern hemisphere and covers approxi-
4 mately 13000 km² area from approximately 48.5°S to 51.5°S (Aniya et al.,
5 1996; Figure 1). The SPI consists of 48 outlet glaciers with an average alti-
6 tude of 1355 m above sea level. All these outlet glaciers, except for two, are
7 calving (Aniya et al., 1996). The ones on the western Chilean side mostly
8 calve into fjords as tidewater calving glaciers, whereas those on the eastern
9 Argentina side terminate into proglacial lakes (Aniya et al., 1996; Warren
10 and Aniya, 1999). Their retreat in the frontal positions and rapid thinning
11 toward the end of the 20th century have been reported, suggesting a signifi-
12 cant contribution to global sea level increases (Aniya et al., 1997; Rignot et
13 al., 2003). Moreover, Gravity Recovery And Climate Experiment (GRACE)

14 observation data recorded since 2002 indicate a total mass loss rate from both
15 the Northern Patagonian Ice Field and the SPI to be ranging from -23.0 ± 9.0
16 Gt a^{-1} to $-26.0\pm 6.0 \text{ Gt a}^{-1}$ (Chen et al., 2007; Ivins et al., 2011; Jakob et
17 al., 2012). GRACE-based mass-loss estimates in the beginning of the 21st
18 century are larger than the corresponding volume loss rate derived in the
19 late 20th century (Rignot et al., 2003). The recently reported surface height
20 change rates, based on a time series of digital elevation models (DEMs), are
21 also consistent with GRACE-based estimates, which indicates an even more
22 rapid drawdown over the past decade (Willis et al., 2012).

23 While near-surface temperature increases associated with global warm-
24 ing presumably contribute to ice loss due to melting, the accelerated ice
25 losses reported on Greenland and Antarctica have been linked to changes in
26 glacier dynamics as well (Rignot and Kanagaratnam, 2006; van den Broeke
27 et al., 2009; Pritchard et al., 2009). In particular, many polar glaciers that
28 calve into the ocean have undergone significant acceleration, known as dy-
29 namic thinning, and have thus further contributed to ice loss. However, re-
30 cent studies demonstrate spatial-temporal complexities of the outlet glacier
31 velocities in Greenland (Moon et al., 2012; Bevan et al., 2012). In contrast
32 to these large polar glaciers, no detailed glacier velocity maps are available
33 for the Patagonian Ice Fields with the exception of those for certain acces-
34 sible glaciers (Naruse et al., 1992, 1995; Stueffer et al., 2007; Sugiyama et
35 al., 2011; Rivera et al., 2012a). Satellite-derived velocity maps are also lim-
36 ited to Glaciars Perito Moreno (Rott et al., 1998; Michel and Rignot, 1999;
37 Ciappa et al., 2010) and Glaciar Upsala (Skvarca et al., 2003; Floricioiu et
38 al., 2008, 2009; Sakakibara et al., 2013). Thus, it remains uncertain if and

39 to what extent dynamic thinning has affected the Patagonian Ice Fields.
40 In this study, we show the spatial and temporal changes in flow velocities
41 at eight major glaciers in the SPI by applying an offset tracking technique
42 to the intensity images of the Environmental Satellite/Advanced Synthetic
43 Aperture Radar (Envisat/ASAR) and Advanced Land Observation Satel-
44 lite/Phased Array-type L-band Synthetic Aperture Radar (ALOS/PALSAR)
45 data recorded from 2002 to 2011. In addition, we used the cloud-free char-
46 acteristics of SAR imagery for examining the terminus changes in order to
47 determine whether the ice acceleration is associated with calving episodes.
48 The examined eight glaciers include Glaciars Upsala, Jorge Montt, Occiden-
49 tal, Pio XI (or Brügger), O’Higgins, Viedma, Perito Moreno, and Grey (Fig-
50 ure 1). We selected these glaciers not only because their sizes were sufficient
51 to be imaged by the spatial resolution of presently available SAR data but
52 also because they were more frequently imaged than others so that we could
53 increase the temporal resolution, which allowed us to detect rapid changes
54 in the ice dynamics.

55 As in the case of Greenland (Moon et al., 2012), we subsequently show
56 that not all of the glaciers reveal ice acceleration and rapid terminus re-
57 treat. Submarine melting has been suggested as a principal triggering mech-
58 anism for the accelerated ice motion in Greenland, because the timing of the
59 glacier’s acceleration coincided with that of ocean water warming near Green-
60 land (Holland et al., 2008; Rignot et al., 2010; Straneo et al., 2011). The
61 rapid retreat and flow acceleration in the SPI, however, occur at both marine
62 and fresh-water terminating glaciers, which suggests the presence of addi-
63 tional general processes independent of water salinity. While the physically

64 based calving model remains elusive (Benn et al., 2007a), we interpret the
65 observed data sets on the basis of the calving model based on crevasse-depth
66 criteria (Benn et al., 2007a, b; Nick et al., 2010).

67 **2. Data and Analysis Method**

68 *2.1. Satellite data*

69 To generate glacier surface velocity maps, we processed the PALSAR im-
70 ages with a wavelength of 23.6 cm recorded from June 2007 to February 2011
71 from ALOS, which was launched in 2006 by the Japan Aerospace Exploration
72 Agency (JAXA) (Table 1, Figure 1). To extend the analysis period further
73 back to 2003, we also used the C-band (wavelength of 5.6 cm) ASAR images
74 from Envisat launched in 2002 by the European Space Agency (Table 1, Fig-
75 ure 1), which often contains de-correlation problems; the advantage of the
76 L-band over C-band was shown before (Rignot, 2008; Strozzi et al., 2008).
77 On the basis of our observations of insignificant temporal velocity changes at
78 Glaciar Perito Moreno (supplementary material), the differences in penetra-
79 tion depths due to different wavelengths do not appear to affect the inferred
80 velocities. This result is theoretically reasonable because the most significant
81 changes in glacier-flow velocity profile are expected to occur near the glacier
82 bed rather than near the surface (Cuffey and Patterson, 2010).

83 The off-nadir beam angle of PALSAR is 34.3° , which forms $\sim 39^\circ$ inci-
84 dent angle at the flat ground in the image center. There are two available
85 imaging modes, fine beam single polarization (FBS, HH) and fine beam dual
86 polarization (FBD; HH and HV). We used data from only HH polarization.
87 The difference between FBS and FBD is the slant range (across track) reso-

88 lution, which is ~ 4.7 m for the FBS mode and ~ 9.4 m for the FBD mode;
89 the azimuth resolution is 3.1 m regardless of the mode. The FBD data are
90 oversampled twice along the range axis. On the other hand, the ASAR data
91 used in this study were obtained along a descending path with a local inci-
92 dence beam angle of $\sim 23^\circ$; the ASAR data from an ascending path of the
93 mode IS6 were used only for the analysis of Glaciar Perito Moreno (Table1,
94 supplementary material). This smaller incidence angle lowers the sensitiv-
95 ity to the east–west component of displacement, although it can increase
96 the sensitivity of the vertical component. The spatial resolution of ASAR
97 in the slant range and azimuth direction is 7.8 m and 4.1 m, respectively.
98 We processed the PALSAR level 1.0 products and ASAR level 0 products to
99 generate single look complex images.

100 *2.2. Pixel-offset tracking*

101 Although the other approaches are available, such as radar interferome-
102 try (Goldstein et al., 1993) and multiple aperture interferometry (Gourmelen
103 et al., 2011), they are based on phase images that will encounter coher-
104 ence loss and phase unwrapping problems to quantify larger displacements.
105 In this study, pixel-offset tracking (intensity tracking or speckle tracking)
106 algorithms, based on maximizing the cross-correlation of the radar image
107 patches, were used to observe surface velocities (Michel et al., 1999; Strozzi
108 et al., 2002; Yasuda and Furuya, 2013). We used the intensity tracking
109 algorithm because it is most suitable for detecting rapidly–flowing glacier
110 velocities with long data acquisition intervals (Strozzi et al., 2002, 2008).
111 Although we experimented with a variety of patch sizes and sampling in-
112 tervals, we eventually deemed a search patch of ~ 500 m (range) \times 600 m

113 (azimuth) area with a sampling interval of $\sim 90 \text{ m} \times 120 \text{ m}$ as optimum
114 parameters. We set a signal-to-noise ratio (SNR) threshold of 4.0; patches
115 below this level were assigned to the missing data. Lower SNR data occur
116 because of the large spatial separation length (Bperp) of the repeating orbits
117 or temporal changes in the surface scattering characteristics; Bperp denotes
118 the perpendicular component of the baseline projected onto the radar line of
119 sight (LOS). Unfortunately, the Bperp for the PALSAR data pairs in summer
120 was relatively long; however, the operational orbit determination accuracy
121 is now approaching sub-meter level with standard errors of tens of centime-
122 ters or less (Scharroo and Visser, 1998; Andersen et al., 1998; Katagiri and
123 Yamamoto, 2008). Moreover, because higher precipitation levels and temper-
124 atures occur in summer, we can consider that snowfall and surface melting
125 lower the cross-correlation between the temporally separated image patches,
126 which prevents derivation of velocity data, particularly in the accumulation
127 zones. We did not mask the non-glacier areas in offset-tracking, because it
128 was important to verify that non-glacier areas could indeed be estimated to
129 be non-deforming, and that there were no artifacts due to topography. The
130 no-displacement signals outside the glaciated areas shown below validated
131 the surface velocity data detected along the glacier itself. Over the glaciated
132 areas, however, we occasionally encountered spurious signals that indicated,
133 for instance, extraordinary fast velocities or physically unrealistic disconti-
134 nities in the velocity distributions. We considered that these spurious data
135 were caused by erroneous matching of objects that actually differed; thus,
136 we visually eliminated such noise.

137 Because the satellite does not repeat exactly the same paths, the effect

138 of fore-shortening also differs in each path, which results in an artifact off-
139 set over rugged terrain (Michel et al., 1999; Sansosti et al., 2006; Kobayashi
140 et al., 2009). We reduced this artifact by applying an elevation-dependent
141 co-registration by employing NASA’s Shuttle Radar Topography Mission
142 (SRTM-4) DEM data with a 3-arcsec resolution, in which the gaps in the
143 original SRTM data were filled (Jarvis et al., 2008). Although the SRTM
144 data may include inherent errors and are nearly a decade old, we used them
145 because there are free of gaps and apparent noise. Because no topography-
146 correlated offsets were apparent, we considered the artifact offset to be ade-
147 quately corrected; it is unlikely that the errors in the SRTM DEM influenced
148 our velocity data.

149 The pixel-offset tracking technique provides range and azimuth offsets,
150 both of which are linear combinations of the three-dimensional (3D) displace-
151 ments. The range offset, U_{ra} , is a projection of the 3D surface displacements
152 onto the slant radar LOS direction, while the azimuth offset, U_{az} , is a projec-
153 tion of the 3D surface displacements along the satellite-track direction. Using
154 the satellite’s heading angle H measured clockwise from the north and the
155 microwave’s incidence angle to the ground I , each offset can be represented
156 as follows:

$$\begin{pmatrix} U_{ra} \\ U_{az} \end{pmatrix} = \begin{pmatrix} \cos H \sin I & -\sin H \sin I & -\cos I \\ \sin H & \cos H & 0 \end{pmatrix} \begin{pmatrix} U_e \\ U_n \\ U_z \end{pmatrix}, \quad (1)$$

157 where U_e , U_n , and U_z are defined as eastward, northward, and upward posi-
158 tive displacements, respectively. The imaging angles and expressions of U_{ra}
159 and U_{az} for each satellite’s observation mode are indicated in Table 2.

160 Because the two displacement maps do not allow us to resolve the 3D
161 displacements, we derived the surface velocity data by using the parallel flow
162 assumption (Joughin et al., 1996). Although either the range or azimuth
163 offset data allow us to derive the surface velocity with the parallel flow as-
164 sumption, we used both data sets to solve the over-determined problem by the
165 least-squares method. The local topographic gradient vector was estimated
166 from the SRTM-4 data. Because only the local flow orientation and slope an-
167 gles are necessary in the argument of trigonometric functions for parallel flow
168 approximation, the ice-thickness changes that may have occurred between
169 the SRTM and PALSAR/ASAR data acquisition would be insignificant as
170 potential error sources in the computation of a unit vector.

171 Although the effects of atmospheric propagation and inaccurate satellite
172 orbit generate significant errors in the InSAR phase data, these errors are
173 insignificant in the offset tracking data. This is because the errors in the offset
174 tracking data are due to those in the image registration, and are larger than
175 those due to atmospheric propagation and satellite orbit (Strozzi et al., 2002).
176 The uncertainties of the offset measurements have been estimated to be ~ 0.3 –
177 0.4 m at the non-deforming rugged terrain in the ALOS/PALSAR data with
178 a 46-day interval (Kobayashi et al., 2009). If the ice is flowing at a constant
179 rate over the data acquisition interval, the error in the velocity estimates
180 can be inferred as 0.005 – 0.01 m/day, and will be inversely proportional to
181 the data acquisition interval (Strozzi et al., 2002). However, errors in pixel-
182 offset tracking can also originate from other sources. The most significant
183 error source is the temporal de-correlation between image patches due to
184 changes in objects' scattering properties. Thus, all the the data pairs shown

185 in this study have the shortest possible 46- and 35-day temporal separation,
186 which denote the PALSAR and ASAR recurrent periods, respectively. The
187 ASAR data more often indicated larger errors, probably because the short
188 wavelength data tend to undergo the de-correlation problem. The magnitude
189 of errors also varies seasonally from less than 5 m/a up to 30 m/a, depending
190 on the season of the SAR data acquisition (Yasuda and Furuya, 2013).

191 For point sites such as those at the Glaciar Upsala and the site C at the
192 Glaciar Jorge Montt, we averaged the velocities at the nearby 500 m^2 area
193 and considered the derived standard deviation as the measurement error,
194 which ranges from less than 0.1 m/day to ~ 0.5 m/day. For transverse veloc-
195 ity profile, we selected five velocity profiles that are closely-located within 100
196 m, and computed the average and standard deviation along the transverse
197 direction. The velocities and error bars for the transverse profiles shown be-
198 low were derived by further averaging the data along the transverse direction;
199 the velocity profiles and errors along the transverse direction are shown in
200 the supplementary material.

201 *2.3. Ice-front position changes*

202 Cloud-free SAR intensity images permit the tracking of ice-front positions
203 over time if clear image contrasts are present between the ice and water sur-
204 faces. By using the original single look complex images, the intensity images
205 were derived by multi-looking in range and azimuth directions. The spatial
206 resolution was 40 m \times 40 m. We visually identified the ice-front positions at
207 each SAR intensity image; we did not perform mechanized automatic detec-
208 tion. The front position change shown below is referenced to the first SAR
209 image in 2002 or 2003, and represents the average change derived by dividing

210 the total area of each polygon by a fixed width of a reference profile in the
211 upstream direction (Moon and Joughin, 2008). Errors in digitized frontal
212 positions arose mainly from our misidentification of the frontal positions,
213 which could be attributed to image resolution and the lower image contrast
214 between the ice and water surfaces. Images with unclear contrasts between
215 the ice and water surfaces were not used in this study. Bevan et al. (2012)
216 evaluated the accuracies of ± 49 m for ERS1/2 and ASAR SAR images. We
217 consider that the accuracies of our identified frontal positions are compara-
218 ble to or better than the Bevan et al's estimate, because the resolution is
219 close to those of ERS1/2 and ASAR in PALSAR's FBD mode and better in
220 PALSAR's FBS mode.

221 **3. Results**

222 Regarding temporal evolution of surface velocities at the eight large glaciers
223 examined in this study from 2003 to 2011, Glaciars Upsala, Jorge Montt,
224 Occidental, and Pio XI revealed significant acceleration of greater than 30
225 %. Although temporal fluctuations possibly due to seasonalities were rec-
226 ognized, no large velocity changes were evident at Glaciars Grey, Perito
227 Moreno, Viedma, and O'Higgins. With the exception of Pio XI, these ac-
228 celerated glaciers also revealed significant retreating in the frontal positions.
229 In this section, we present the observation results of the Glaciars Upsala,
230 Jorge Montt, Occidental, and Pio XI; the results of the remaining glaciers
231 are shown in the supplementary material.

232 *3.1. Glaciar Upsala*

233 Glaciar Upsala, the third largest glacier in the SPI, contains three ter-
234 mini, of which the westernmost terminus is the largest and calves into Brazo
235 Upsala of Lago Argentino (Skvarca et al., 2003). The water depth is 400–
236 500 m (Naruse and Skvarca, 2000). A rapid retreat of the frontal position
237 since 1978 has been reported (Aniya and Skvarca, 1992; Skvarca et al., 1995;
238 Naruse et al., 1997; Naruse and Skvarca, 2000; Skvarca et al., 2002). The
239 thinning rate near the glacier front was reported to be 11 m/a between 1990
240 and 1993 (Skvarca et al., 1995) and 10 ± 2 m/a between 2000 and 2005 (Willis
241 et al., 2012), but accelerated to 24.8 ± 2.4 m/a between 2005 and 2011 (Willis
242 et al., 2012). Annual velocities near the terminus based on satellite imagery
243 were first derived by Skvarca et al (2003), who applied a cross-correlation
244 method to Landsat 7 Enhanced Thematic Mapper Plus (ETM+) images
245 acquired between 2000 and 2001; this approach is similar to the currently
246 used intensity tracking approach. Near the fastest-flowing western terminus,
247 Skvarca et al (2003) derived average velocities of approximately 1600 m/a,
248 equivalent to 4.4 m/day, which were in good agreement with the field mea-
249 surement obtained in 1995 (Skvarca et al., 1995). Sakakibara et al (2013)
250 extended the analysis period to 2011. On the basis of TerraSAR-X data
251 acquired between December 2007 and January 2008, Floricioiu et al (2008)
252 reported a maximum velocity of 5.6 m/day, which is significantly faster than
253 the earlier observations in 1995 and 2001; Floricioiu et al (2009) extended the
254 study period. However, the time at which the glacier initiated acceleration
255 and the evolution of the frontal positions remain unknown.

256 Surface velocities near the terminus position could not be derived in this

257 study because of the low SNR in the offset tracking near the ice front. We con-
258 sider that the faster ice motion near the terminus caused significant temporal
259 changes in the surface features and hence their scattering characteristics; the
260 46/35-day acquisition intervals in PALSAR/ASAR are too long for tracking
261 the surface features of such a rapidly flowing region with sufficient correla-
262 tion. However, the slower velocity data in the upstream could be derived;
263 thus, we examined the temporal changes in velocities at two sites closer to the
264 terminus (A and B in Figure 2a), in which the velocity data were acquired as
265 frequently as possible. We averaged the velocities at 36 pixels (over 500 m^2)
266 for each site and assigned their standard deviations as the error bar in Figure
267 2b. One site was in the main stream of Glaciar Upsala, and the other was
268 in Glaciar Bertachi, one of the western tributaries closest to the frontal posi-
269 tion. Figure 2b summarizes the temporal evolution of both surface velocities
270 at the two sites and frontal positions derived in this study. Figure 3 shows
271 the terminus locations visually identified over time. Although we could not
272 generate useful velocity data between 2006 and 2010 because of a satellite
273 orbit problem, we observed a nearly 180 % velocity increase between 2005
274 and 2010 even at a point 7 km from the terminus in the main stream. From
275 2003 to 2005, the near-terminus velocities were 2 m/day, which are in agree-
276 ment with Skvarca et al's observations in 2001 (Skvarca et al 2003). Even in
277 Glaciar Bertachi, it is evident that the 2010 surface velocities are nearly 200
278 % those of the 2003–2005 data. In 2010–2011, therefore, the near-terminus
279 region is apparently flowing faster than previously recorded speeds. The
280 frontal position retreated nearly 3.5 km from 2002 to 2011 and approached
281 the lower end of Glaciar Bertachi. The speed up on Bertacchi between July

282 2010 and January 2011 may be associated with the recent retreat. Although
283 the point A seems stable in Figure 2b, it is likely that the similar speed-up at
284 point A occurred but was not detected by the available data. In view of the
285 TerraSAR-X intensity image in Floricioiu et al (2008), the frontal position in
286 January 2008 was close to that recorded in 2005. While the front gradually
287 retreated from 2002 to 2005 with possible seasonal fluctuations (Figure 3),
288 the retreating appears to have accelerated in August 2008.

289 *3.2. Glaciar Jorge Montt*

290 Glaciar Jorge Montt is located at the northern end of the SPI and calves
291 into an unnamed fjord that opened as a result of its glacier retreat to a
292 maximum of 19.5 km from 1898 to 2011 (Rivera et al., 2012b). The maximum
293 thinning rate was estimated to be 17.9 m/a between 1975 and 2000 (Rignot
294 et al., 2003) and 21.5 ± 0.8 m/a between 2000 and 2012 (Willis et al., 2012).
295 In addition, the rate of glacier terminus retreat was estimated to be 200 m/a
296 between 2001 and 2011 (Willis et al., 2012).

297 So far, few surface velocity measurements of Glaciar Jorge Montt have
298 been reported. Rivera et al (2012a) derived an average velocity of 13 ± 4
299 m/day for the near-terminus region between 2010 and 2011 by using both
300 ground-based cameras and a feature tracking based on ASTER images. Com-
301 paring Rignot et al's unpublished velocity data derived from the 2004 C-band
302 Radarsat-1 images, Rivera et al (2012a) suggested an acceleration between
303 2004 and 2010. However, the surface velocity data in the other years and
304 up-glacier parts remain uncertain.

305 Figure 4a shows an example of a velocity map derived from data ac-
306 quired between January and February 2008. Although we could not derive

307 the velocity data near the terminus region as was the case for Glaciar Up-
308 sala, the derived velocity maps complement the observations of Rivera et al
309 (2012a), because our velocity maps cover the middle to upstream regions of
310 the glaciers. Figure 4b summarizes the temporal evolutions of both frontal
311 location changes and the mean velocities at one flow velocity profile (A–B in
312 Figure 4a) and the other upstream site (C in Figure 4a). While the mean
313 value of the A–B profile is smaller than the mean at the C, this is due to
314 the averaging procedure, and the flow velocity at the center of A–B profile
315 is higher than at C; the velocities and errors along the transverse profile are
316 shown in the supplementary. The measured velocity profile is located 5.5 km
317 upstream from that measured by Rivera et al (2012a). Figure 5 indicates
318 the frontal locations identified at each epoch. The relationship between the
319 retreating rate and flow velocities from 2003 to 2007 remains uncertain be-
320 cause not all of the image pairs allowed us to derive the flow velocity data.
321 However, both the retreating rate and flow velocities are not constant over
322 time. Although the frontal position continued to retreat since 2003, it became
323 stagnant from 2007 to 2008 when the flow velocities significantly decreased.
324 From 2008 onward, the retreating rate apparently accelerated, indicating
325 ~ 470 m/a, and the flow velocities in 2011 increased by 130 %, compared to
326 those recorded in 2003. While the flow acceleration reported by Rivera et
327 al (2012a) was derived by comparing the data acquired in 2004 and 2010,
328 Figure 4b suggests that the acceleration was initiated in 2008.

329 *3.3. Glaciar Occidental*

330 Glaciar Occidental is located on the western side of the SPI and flows into
331 a proglacial lake. On the basis of the analysis of Landsat TM and Advanced

332 Visible and Near Infrared Radiometer-2 (AVNIR-2) on ALOS images, the
333 terminus retreat between 1986 and 2006 was estimated to be 1.1 km, and
334 the terminus shape was found to be disintegrated (JAXA, 2010). Regarding
335 surface elevation change rate, Glaciar Occidental is also thinning at a rate of
336 2–5 m/a (Willis et al., 2012). To our knowledge, however, no flow velocity
337 data have been published so far.

338 We selected two transverse profiles at downstream and upstream posi-
339 tions (A–B and C–D, respectively, in Figure 6a). In contrast to the rapidly
340 flowing glaciers previously described, this glacier allowed us to derive flow
341 velocity data even near the terminus, likely because the slower flow veloci-
342 ties allowed the glacier to maintain its surface features over time. Figure 6b
343 summarizes the temporal evolution of mean velocities at each profile and
344 the frontal position; temporal evolution of the velocity profile is shown in
345 the supplementary material. While the velocities in the upstream were sta-
346 ble over time (C–D), those near the terminus in 2008–2010 have apparently
347 increased by more than 200 % over 2004–2005. The near-terminus region ap-
348 parently underwent a significant longitudinal stretching. We evaluated the
349 frontal position retreat to be ~ 2 km from 2004 to 2011. However, the frontal
350 positions at some epochs are missing because a vague image contrast pre-
351 vented clear identification. Instead of a clear frontal position, we observed
352 numerous icebergs that likely disintegrated from the terminus. The rate of
353 terminus retreat accelerated from 55 m/a for the period from 1986 to 2006
354 to ~ 285 m/a for the recent period from 2004 to 2011.

355 *3.4. Glacier Pio XI*

356 Glaciar Pio XI, the largest glacier in the SPI, flows to the west from
357 a location near Volcán Lautaro (elevation 3380 m) and bifurcates into two
358 tongues to the north and south near its lower end, which flow into 'Lago
359 Greve' and Eyre Fjord, respectively (Figure 7a); the southern front is thus a
360 tidewater front. In contrast to the other glaciers in Patagonia that are rapidly
361 retreating, Glaciar Pio XI was known for its significant terminus advances
362 at both tongues during the 20th century (Warren and Rivera, 1994; Rivera
363 et al., 1997). The front region is reportedly thickening at a rate of greater
364 than 2 m/a (Rivera and Casassa, 1999; Willis et al., 2012). On the basis of
365 ground-based measurements recorded in November 1995, Rivera et al. (1997)
366 reported maximum velocities of 17 to 50 m/day near the southern terminus.
367 Although these faster velocities, in addition to the terminus advances, have
368 led to an interpretation of a surging glacier, the factors controlling the dy-
369 namics of Glaciar Pio XI remain uncertain (Rivera et al., 1997). Apparently,
370 this glacier has not been directly responding to the climate change (Warren
371 and Rivera, 1994).

372 We selected three profiles across the northern tongue (A–B in Figure 7a),
373 southern tongue (C–D in Figure 7a), and the main upstream region (E–F
374 in Figure 7a) to reveal the temporal evolution of the surface velocities. Fig-
375 ures 7b–7d summarize the temporal evolution of the mean surface velocities
376 at each profile, and the frontal position changes at the northern and southern
377 tongues from 2003 to 2011 are shown in Figures 7b and 7c. The temporal
378 evolution of each velocity profile is shown in the supplementary material. The
379 flow velocity in the main upstream was relatively stable over time, although

380 it revealed deceleration in 2007 (Figure 7d). In contrast, the velocities at the
381 northern and southern tongues were highly variable over time (Figures 7b
382 and 7c). The southern tongue reveals faster signals in 2003, 2005, and 2007,
383 when the velocities nearly doubled those in slower phases. While the northern
384 tongue was slowly flowing at 0.2 m/day in 2003, it gradually accelerated and
385 reached 2.0 m/day in 2007. The upstream thus does not appear to directly
386 control the flow velocities in the downstream.

387 Despite the highly variable velocity changes to the northern and southern
388 tongues (Figures 7b and 7c), we did not observe any significant retreat as
389 observed in Glaciars Upsala, Jorge Montt, and Occidental. Figure 8 includes
390 the frontal positions over the analyzed period. While these positions have
391 overall advanced from 2003 to 2011, we observed fluctuations in the front
392 positions within a range of ~ 250 m between advancing and retreating periods.

393 4. Discussion and Conclusion

394 Although the retreat and thinning of glaciers in the SPI over the past
395 decades have been well-documented, we used SAR image analysis to demon-
396 strate that not all of the examined glaciers revealed significant changes in
397 frontal positions and flow velocities from 2002 to 2011. Moreover, even for
398 such glaciers that underwent rapid retreat and acceleration, the terminus re-
399 treat and flow acceleration occurred sporadically rather than gradually over
400 time, suggesting that positive-feedback processes promoted such movement.
401 This finding was made possible through the use of SAR images that were
402 free from cloud and night time problems, although more frequent image ac-
403 quisitions are desirable.

404 The observed rapid retreat and acceleration at Glaciars Upsala, Jorge
405 Montt, and Occidental have important implications for calving mechanisms.
406 In particular, despite the marked differences in absolute flow velocity among
407 the three glaciers, the region toward the terminus at each glacier underwent
408 significant acceleration, which was observed by calculating differences in the
409 velocity map at two epochs (Figure 9). Figure 9 indicates larger velocity
410 increments downstream, which demonstrates longitudinal stretching or ex-
411 tension toward the termini. Because longitudinal stretching is observed even
412 at distances greater than ~ 5 km upstream from the 2011 termini, the actual
413 accelerations near the terminus regions of Glaciars Upsala and Jorge Montt
414 will probably be much larger (Figures 9a and 9b). The near-terminus area
415 in Glaciar Occidental flowed at a rate of ~ 0.5 m/day by at least 2005 and
416 began to accelerate in 2007, while the upstream velocities were stable. Such
417 longitudinal stretching toward the terminus is clearly revealed at Glaciar
418 Occidental (Figure 9c).

419 The observed longitudinal stretching at the rapidly retreating glaciers will
420 contribute to increasing the crevasse-depths, and thus appears to support a
421 calving model based on crevasse-depth criteria (Benn et al., 2007a, b; Nick
422 et al., 2010), in which the absolute flow velocity itself is not critical. Benn et
423 al. (2007b) proposed that longitudinal stretching due to the spatial velocity
424 gradient, which determines the location and depth of surface crevasses, and
425 the difference between ice thickness and water depth (effective pressure) are
426 the primary controls for the frontal position of calving. This theory assumes
427 that the basal sliding velocity is equal to the vertically averaged ice velocity.
428 While Benn et al's model predicts the calving front position in which the

429 depth of the surface crevasse equals the ice height above the water line, Nick
430 et al. (2010) modified the model to predict calving for cases in which both
431 surface and basal crevasses penetrate the full thickness of the glacier.

432 The longitudinal stretching and rapid terminus retreat at Glaciar Upsala,
433 Jorge Montt, and Occidental can be regarded as indicators of the on-going
434 dynamic thinning process. These three glaciers have been thinning over
435 the past decade (Willis et al., 2012). Because the glacier thinning reduces
436 the viscous ice velocity due to the decrease of gravitational force, we at-
437 tribute the observed speed-up to the enhanced basal sliding velocity. We
438 consider that the basal sliding enhancement is caused by the surface melt
439 input and subsequent reduction of effective pressure due to the water pres-
440 sure increase as observed at Greenland (e.g., Sundal et al., 2011). If the
441 basal sliding velocity dominantly contributes to the vertically averaged ve-
442 locity, the longitudinal stretching will also increase and allow the crevasses
443 to penetrate further, causing the terminus to retreat up-glacier. As recog-
444 nized from a bathymetric survey conducted at Glaciar Upsala (Naruse and
445 Skvarca, 2000), this terminus retreat will likely be halted in shallower water
446 because the effective pressure will increase. Such stabilization of the ter-
447 minus retreat is, however, not simply controlled by the local water-depth or
448 ice thickness as in the height-above-buoyancy model by Van der Veen (1996).
449 Physics-based crevasse-depth calving criteria can eliminate the unrealistically
450 large terminus retreats predicted from the height-above-buoyancy criterion
451 (Nick et al., 2010).

452 Our observations suggest that even other seemingly stable glaciers be-
453 tween 2003 and 2011 may undergo rapid retreat and acceleration in the fu-

454 ture. The Glaciar Occidental observation provides an important lesson for
455 understanding the sporadic nature of calving processes. However, we cannot
456 determine the point at which glaciers will undergo significant frontal retreat
457 and acceleration in the future because calving processes involve a variety of
458 unknown variables, which remain poorly understood (Benn et al., 2007a).
459 Continuation of frequent surface velocity monitoring and combining the re-
460 sults with bathymetric and ice-thickness survey data can more precisely val-
461 idate and refine the calving model, which may enable prediction of the initi-
462 ation of dynamic-thinning.

463 The behavior of Glaciar Pio XI is enigmatic, and has been suggested as
464 a surging type (Rivera et al., 1997). Transverse velocity profiles derived in
465 this study indicate parabolic shapes with smaller velocities near the edge,
466 which increase toward the center and do not exhibit the plug flow observed
467 in other surging glaciers (Kamb et al., 1985; Murray et al., 2003; Yasuda and
468 Furuya, 2013). However, note that the maximum water depths in front of
469 the calving front at Eyre Fjord are ~ 20 m, and that those at Lago Greve
470 are speculated to be much shallower than 150 m (Warren and Rivera, 1994).
471 These water depths are significantly shallower than those at other glaciers,
472 which may be attributed to the former surging episodes that should have
473 transported a sufficient amount of sediments to raise the bottom depth of
474 the fjord. While it appears unlikely that a rapid terminus retreat will begin
475 in the near future, it is important to continue monitoring Glaciar Pio XI with
476 the same frequency as that of other calving glaciers in the SPI.

477 It remains uncertain how much the total ice loss in the Patagonian Ice
478 Fields is split into surface processes (runoff and precipitation) and ice dynam-

479 ics, and the surface velocity data are indispensable to evaluate the contribu-
480 tion from ice dynamics. The velocities presented in this study are still not
481 complete, because the velocities at the very front of the glaciers are missing.
482 Because the missing velocities near the front are probably faster, the inferred
483 ice velocities might be helpful to constrain the lower bound of ice discharge.
484 Nonetheless, given the fact that not all the examined glaciers revealed accel-
485 eration and terminus retreat, the contribution from ice dynamics to the total
486 ice loss might be not as high as those in Greenland, where widespread ice
487 acceleration was observed (Joughin et al., 2008) and the partitioning ratio
488 was shown to be equal (van den Broeke et al., 2009). In order to quantify
489 the ice discharge, both surface mass balance and ice thickness data in the
490 Patagonian Ice Fields are also necessary.

491 **5. Acknowledgements**

492 PALSAR level 1.0 data in this study were provided by the PALSAR
493 Interferometry Consortium to Study our Evolving Land surface (PIXEL)
494 and the ALOS 3rd PI project under cooperative research contracts with
495 JAXA. The PALSAR data are owned by JAXA and the Ministry of Economy,
496 Trade and Industry. Envisat data are copyrighted by ESA and were provided
497 under Cat-1 project 9364. This study is partially supported by KAKENHI
498 (24651001). We acknowledge two anonymous reviewers for their helpful and
499 constructive comments.

500 **References**

501 Andersen, P. H., K. Aksnes, & H. Skonnord. (1998). Precise ERS-2 orbit de-
502 termination using SLR, PRARE, and RA observations, *J. Geodesy*, 72(7/8),
503 421–429.

504 Aniya, M. & P. Skvarca. (1992). Characteristics and variations of Upsala
505 and moreno glaciers, southern patagonia, *Bull. Glacier Res.*, 10, 39–53.

506 Aniya, M., H. Sato, R. Naruse, P. Skvarca, & G. Casassa. (1996). The
507 Use of Satellite and Airborne Imagery to Inventory Outlet Glaciers of the
508 Southern Patagonia Icefield, South America, *Photogramm. Eng. Remote*
509 *Sens.*, 62(12), 1361–1369.

510 Aniya, M., H. Sato, R. Naruse, P Skvarca, & G. Casassa. (1997). Recent
511 Glacier Variations in the Southern Patagonia Icefield, South America, *Arct.*
512 *Alp. Res.*, 29, 1–12.

513 Benn, D. I., C. R. Warren, & R. H. Mottram. (2007a). Calving pro-
514 cesses and the dynamics of calving glaciers, *Earth Sci. Rev.*, 82, 143–179,
515 doi:10.1016/j.earscirev.2007.02.002.

516 Benn, D. I., N. R. J. Hulton, & R. H. Mottram. (2007b). 'Calving laws',
517 'sliding laws' and the stability of tidewater glaciers, *Ann. Glaciol.* 46, 123–
518 130.

519 Bevan, S. L., T. Murray, A. J. Luckman, E. Hanna, & P. Huy-
520 brechts. (2012). Stable dynamics in a Greenland tidewater glacier over
521 26 years despite reported thinning, *Ann. Glaciol.*, 53(60), 241–248, doi:
522 10.3189//2102AoG60A076.

523 Chen, J. L., C. R. Wilson, B. D. Tapley, D. D. Blankenship, & E. R.
524 Ivins. (2007). Patagonia Ice Field melting observed by Gravity Recov-
525 ery and Climate Experiment (GRACE), *Geophys. Res. Lett.*, 34, L22501,
526 doi:10.1029/2007GL031871.

527 Ciappa, A., L. Pietranera, & F. Battazza. (2010). Perito Moreno Glacier
528 (Argentina) flow estimation by COSMO SkyMed sequence of high-resolution
529 SAR-X imagery, *Remote Sens. Environ.*, 114, 2088–2096.

530 Cuffey, K. M., & W. S. B. Paterson. (2010). *The Physics of Glaciers*, 4th
531 ed., Elsevier.

532 Delgado, S. (2009). GLIMS Glacier Database. Boulder, CO: National Snow
533 and Ice Data Center/World Data Center for Glaciology. Digital Media.

534 Dickmann, N. (2007). GLIMS Glacier Database. Boulder, CO: National
535 Snow and Ice Data Center/World Data Center for Glaciology. Digital Media.

536 Floricioiu, D., M. Eineder, H. Rott, & T. Nagler. (2008). Velocities of Major
537 Outlet Glaciers of the Patagonia Icefield Observed by TerraSAR-X, *Proc.*
538 *IGARSS 2008*, IV - 347 - IV - 350 , doi: 10.1109/IGARSS.2008.4779729.

539 Floricioiu, D., M. Eineder, H. Rott, N. Yague-Martinez, & T. Nagler. (2009).
540 Surface velocity and variations of outlet glaciers of the Patagonia Icefields
541 by means of TerraSAR-X, *Proc. IGARSS 2009*, II - 1028 - II - 1031, doi:
542 10.1109/IGARSS.2009.5418279

543 Goldstein, R. M., H. Engelhardt, B. Kamb, & R.M. Frolich. (1993). Satellite
544 radar interferometry for monitoring ice sheet motion: application to an
545 Antarctic ice stream, *Science*, 262 (5139), 1525–1530.

546 Gourmelen, N., S. W. Kim, A. Shepherd, J. W. Park, A. V. Sundal, H.
547 Björnsson, and F. Pálsson (2011), Ice velocity determined using conven-
548 tional and multiple-aperture InSAR, *Earth Planet. Sci. Lett.*, 307, 156–160,
549 doi:10.1016/j.epsl.2011.04.026.

550 Holland, D. M., R. H. Thomas, B. de Young, M. H. Ribergaard, & B. Ly-
551 berth. (2008). Acceleration of Jakobshavn Isbr triggered by warm subsurface
552 ocean waters, *Nat. Geosci.*, 1, 659–664, doi:10.1038/ngeo316.

553 Ivins, E. R., M. M. Watkins, D. N. Yuan, R. Dietrich, G. Casassa,
554 & A. Rülke. (2011). On-land ice loss and glacial isostatic adjustment
555 at the Drake Passage; 2003–2009, *J. Geophys. Res.*, 116, B02403,
556 doi:10.1029/2010JB007607.

557 Jarvis A., H. I. Reuter, A. Nelson, & E. Guevara. (2008). Hole-filled seam-
558 less SRTM data V4, International Centre for Tropical Agriculture (CIAT),
559 available from <http://srtm.csi.cgiar.org>.

560 Jacob, T., J. Wahr, W. T. Pfeffer, & S. Swenson. (2012). Recent con-
561 tributions of glaciers and ice caps to sea level rise, *Nature* 482, 514–518,
562 doi:10.1038/nature10847

563 JAXA. (2010). Significant retreats of huge glaciers
564 in Patagonia, South America (Part 3). available at
565 <http://www.eorc.jaxa.jp/en/imgdata/topics/2010/tp100421.html>

566 Joughin, I., R. Kwok, & M. Fahnestock. (1996). Estimation of ice-sheet
567 motion using satellite radar interferometry: Method and error analysis with
568 application to Humboldt Glacier, Greenland, *J. Glaciol.*, 42, 564–575.

- 569 Joughin, I., S. B. Das, M. A. King, D. E. Smith, I. M. Howat, & T. Moon.
570 (2008). Seasonal Speedup Along the Western Flank of the Greenland Ice
571 Sheet, *Science*, 320, 781–783, doi:10.1126/science.1153288
- 572 Kamb, B., C. F. Raymond, W. D. Harrison, H. Engelhardt, K. A.
573 Echelmeyer, N. Humphrey, M. M. Brugman, & T. Pfeffer. (1985). Glacier
574 surge mechanism: 1982–1983 surge of Variegated Glacier, Alaska, *Science*,
575 227, 469–479.
- 576 Katagiri, S. & Y. Yamamoto. (2008). Technology of precise orbit determi-
577 nation, *Fujitsu Sci. Tech. J.*, 44(4), 401–409.
- 578 Kobayashi, T., T. Takada, M. Furuya, & M. Murakami. (2009). Lo-
579 cations and types of ruptures involved in the 2008 Sichuan earthquake
580 inferred from SAR image matching, *Geophys. Res. Lett.*, 36, L07302,
581 <http://dx.doi.org/10.1029/2008GL036907>.
- 582 Masiokas, M. (2009). GLIMS Glacier Database. Boulder, CO: National
583 Snow and Ice Data Center/World Data Center for Glaciology. Digital Me-
584 dia.
- 585 Masiokas, M. (2010). GLIMS Glacier Database. Boulder, CO: National
586 Snow and Ice Data Center/World Data Center for Glaciology. Digital Me-
587 dia.
- 588 Michel, R., J.-P. Avouac, & J. Taboury. (1999). Measuring ground displace-
589 ments from SAR amplitude images: Application to the Landers Earthquake,
590 *Geophys. Res. Lett.*, 26, 875–878.

- 591 Michel, R., & E. Rignot. (1999). Flow of Glacier Moreno, Argentina, from
592 repeat-pass Shuttle Radar images: Comparison of the phase correlation
593 method with radar interferometry, *J. Glaciol.*, 45(149), 93–100.
- 594 Moon, T., & I. Joughin. (2008). Changes in ice front position on Green-
595 land’s outlet glaciers from 1992 to 2007, *J. Geophys. Res.*, 113, F02022,
596 doi:10.1029/2007JF000927.
- 597 Moon, T., I. Joughin, B. Smith, & I. Howat. (2012). 21st-Century Evolu-
598 tion of Greenland Outlet Glacier Velocities, *Science*, 336, 576–578, doi:
599 10.1126/science.1219985
- 600 Murray, T., T. Strozzi, A. Luckman, H. Jiskoot, & P. Christakos. (2003). Is
601 there a single surge mechanism? Contrasts in dynamics between glacier
602 surges in Svalbard and other regions, *J. Geophys. Res.*, 108, B52237,
603 doi:10.1029/2002JB001906.
- 604 Naruse, R., P. Skvarca, T. Kadota, & K. Koizumi. (1992). Flow of Upsala
605 and Moreno Glaciers, southern Patagonia, *Bull. Glacier Res.*, 10, 55-62.
- 606 Naruse, R., P. Skvarca, K. Satow, Y. Takeuchi, & K. Nishida. (1995). Thick-
607 ness change and short-term flow variation of Moreno Glacier, Patagonia.
608 *Bull. Glacier Res.*, 13, 21-28.
- 609 Naruse, R., P. Skvarca, & Y. Takeuchi. (1997). Thinning and retreat of
610 Glaciar Upsala, and an estimate of annual ablation changes in southern
611 Patagonia, *Ann. Glaciol.*, 24, 38–42.

- 612 Naruse, R., & P. Skvarca. (2000). Dynamic Features of Thinning and Re-
613 treating Glaciar Upsala, a Lacustrine Calving Glacier in Southern Patago-
614 nia, *Arct. Antarct. Alp. Res.*, 32(4), 485–491.
- 615 Nick, F. M., C. J. van der Veen, A. Vieli, & D. I. Benn. (2010).
616 A physically based calving model applied to marine outlet glaciers
617 and implications for the glacier dynamics, *J. Glaciol.*, 56, 781–794,
618 doi:10.3189/002214310794457344.
- 619 Pritchard, H. D., R. J. Arthern, D. G. Vaughan & L. A. Edwards. (2009),
620 Extensive dynamic thinning on the margins of the Greenland and Antarctic
621 ice sheets, *Nature*, 461, 971–975, doi:10.1038/nature08471.
- 622 Rignot, E., A. Rivera, & G. Casassa. (2003). Contribution of the Patagonia
623 Icefields of South America to Sea Level Rise, *Science*, 302 (5644), 434–437.
- 624 Rignot, E. & P. Kanagaratnam. (2006). Changes in the Velocity Struc-
625 ture of the Greenland Ice Sheet, *Science*, 311, 986–990, doi: 10.1126/sci-
626 ence.1121381
- 627 Rignot, E. (2008). Changes in West Antarctic ice stream dynamics ob-
628 served with ALOS PALSAR data, *Geophys. Res. Lett.*, 35, L12505,
629 doi:10.1029/2008GL033365.
- 630 Rignot, E., M. Koppes, & I. Velicogna. (2010). Rapid submarine melting
631 of the calving faces of West Greenland glaciers. *Nat. Geosci.*, 3, 187–191,
632 doi:10.1038/ngeo765.
- 633 Rivera, A. & Casassa, G. (1999). Volume changes on Pio XI glacier, Patag-
634 onia: 1975–1995, *Global Planet. Change*, 22, 233–244

- 635 Rivera, A., H. Lange, J. C. Aravena, & G. Casassa. (1997). The 20th-century
636 advance of Glacier Pio XI, Chilean Patagonia, *Ann. Glaciol.*, 24, 66–71
- 637 Rivera, A., J. Corripio, C. Bravo, & S. Cisternas. (2012a). Glaciar Jorge
638 Montt (Chilean Patagonia) dynamics derived from photos obtained by fixed
639 cameras and satellite image feature tracking, *Ann. Glaciol.*, 53(60), 147–155,
640 doi:10.3189/2012AoG60A152.
- 641 Rivera, A., M. Koppes, C. Bravo, & J. C. Aravena. (2012b). Little Ice Age
642 advance and retreat of Glaciar Jorge Montt, Chilean Patagonia, *Clim. Past*,
643 8, 403–414, doi:10.5194/cp-8-403-2012
- 644 Rott, H., M. Stuefer, A. Siegel, P. Skvarca, & A. Eckstaller. (1998). Mass
645 fluxes and dynamics of Moreno Glacier, Southern Patagonia Icefield, *Geo-*
646 *phys. Res. Lett.*, 25(9), 1407–1410.
- 647 Sakakibara, D., S. Sugiyama, T. Sawagaki, S. Marinsek, & P. Skvarca.
648 (2013). Rapid retreat, acceleration and thinning of Glaciar Upsala, South-
649 ern Patagonia Icefield, initiated in 2008, *Ann. Glaciol.*, 54(63), 131–138,
650 doi:10.3189/2013AoG63A236.
- 651 Sansosti, E., P. Bernardino, M. Manunta, F. Serafino, & G. Fornaro. (2006).
652 Geometrical SAR Image Registration, *IEEE Trans. Geosci. Rem. Sens.*,
653 44(10), 2861–2870.
- 654 Scharroo, R & P. Visser. (1998). Precise orbit determination and gravity field
655 improvement for the ERS satellites, *J. Geophys. Res.*, 103(C4), 8113–8128
- 656 Skvarca, P., K. Satow, R. Naruse & J.C. Leiva. (1995). Recent thinning,
657 retreat and flow of Upsala Glacier, Patagonia, *Bull. Glacier Res.*, 13, 11–20.

- 658 Skvarca, P., B. Raup, & H. De Angelis. (2002). Calving rates in fresh water:
659 new data from southern Patagonia, *Ann. Glaciol.*, 34, 379–384.
- 660 Skvarca, P., B. Raup, & H. De Angelis. (2003). Recent behaviour of Glacier
661 Upsala, a fast-flowing calving glacier in Lago Argentino, southern Patago-
662 nia, *Ann. Glaciol.*, 36, 184–188.
- 663 Straneo, F., R. G. Curry, D. A. Sutherland, G. S. Hamilton, C. Cenedese,
664 K. Vge & L.A. Stearns. (2011). Impact of fjord dynamics and glacial
665 runoff on the circulation near Helheim Glacier, *Nat. Geosci.*, 4, 322–327,
666 doi:10.1038/ngeo1109
- 667 Strozzi, T., A. Luckman, T. Murray, U. Wegmüller, & C. Werner. (2002).
668 Glacier motion estimation using SAR offset-tracking procedures, *IEEE*
669 *Trans. Geosci. Rem. Sens.*, 40(11), 2384–2391.
- 670 Strozzi, T., A. Kouraev, A. Wiesmann, U. Wegmüller, A. Sharov, and C.
671 L. Werner (2008), Estimation of Arctic glacier motion with satellite L-band
672 SAR data, *Remote Sens. Environ.*, 112, 636–645.
- 673 Stueffer, M., H. Rott, & P. Skvarca. (2007). Glaciar Perito Moreno, Patag-
674 onia: climate sensitivities and glacier characteristics preceding the 2003/04
675 and 2005/06 damming events, *J. Glaciol.*, 53(180), 3–16.
- 676 Sugiyama, S., P. Skvarca, N. Naito, H. Enomoto, S. Tsutaki, K. Tone, S.
677 Marinsek, & M. Aniya. (2011). Ice speed of a calving glacier modulated
678 by small fluctuations in basal water pressure, *Nat. Geosci.*, 4, 597–600,
679 doi://10.1038/ngeo1218.

- 680 Sundal, A. V. et al. (2011), Melt-induced speed-up of Greenland ice
681 sheet offset by efficient subglacial drainage, *Nature*, 469, 521–524, doi:
682 10.1038/nature09740.
- 683 Warren, C., & A. Rivera. (1994). Non-linear climatic response of Calv-
684 ing Glaciers: A case study of Pio XI Glacier, Chilean Patagonia, *Revista*
685 *Chilena de Historia Natural*, 67, 385–394.
- 686 Warren, C., & M. Aniya. (1999). The calving glaciers of southern South
687 America, *Global Planet. Change*, 22, 59–77.
- 688 Willis, M. J., A. K. Melkonian, M. E. Pritchard, & A. Rivera. (2012). Ice
689 loss from the Southern Patagonian Ice Field, South America, between 2000
690 and 2012, *Geophys. Res. Lett.*, 39, L17501, doi:10.1029/2012GL053136.
- 691 van den Broeke, M., J. Bamber, J. Ettema, R. Rignot, E. Schrama, W.
692 J. van de Berg, E. van Meijgaard, I. Velicogna, & B. Wouters. (2009).
693 Partitioning Recent Greenland Mass Loss, *Science*, 326, 984–986, doi:
694 10.1126/science.1178176
- 695 van der Veen, C. J. (1996). Tidewater calving. *J. Glaciol.*, 42(141), 375–385.
- 696 Yasuda, T., & M. Furuya. (2013). Short-term glacier velocity changes at
697 West Kunlun Shan, Northwest Tibet, detected by Synthetic Aperture Radar
698 data, *Remote Sens. Environ.*, 128, 87–106, doi: 10.1016/j.rse.2012.09.021.

Figure 1: Elevation map of the studied area and the glaciers in the South Patagonian Icefield; the elevation data set was obtained NASA’s Shuttle Radar Topography Mission (SRTM). Red triangles represent the termini of the eight analyzed glaciers. Blue and light-blue indicate fjord and proglacial lakes, respectively. Glacier outlines were determined on the basis of the Global Land Ice Measurements from Space (GLIMS) dataset, which is available through the US National Snow and Ice Data Center (Dickman, 2007; Delgado, 2009; Masiokas, 2009, 2010; Davies, 2012).

Figure 2: (a) Spatial distribution of surface flow velocities at Glaciar Upsala, derived from PALSAR images obtained on January 4 and February 19, 2011. (b) Temporal changes in the average frontal position and velocities at sites A and B depicted in (a).

Figure 3: Temporal evolution of the frontal position at Glaciar Upsala between 2002 and 2011. Background is a PALSAR-based scattering intensity image acquired on February 19, 2011.

Figure 4: (a) Spatial distribution of surface flow velocities at Glaciar Jorge Montt, derived from PALSAR images obtained on January 11 and February 26, 2008. (b) Temporal changes in the average frontal position and velocities at profile A–B and site C in (a).

Figure 5: Temporal evolution of the frontal position at Glaciar Jorge Montt between 2002 and 2011. Background is a PALSAR-based scattering intensity image acquired on February 19, 2011.

Figure 6: (a) Spatial distribution of surface flow velocities at Glaciar Occidental, derived from PALSAR images obtained on January 4 and February 19, 2011. (b) Temporal changes in the average frontal position and velocities at profile A–B and site C–D in (a).

Figure 7: (a) Spatial distribution of surface flow velocities at Glaciar Pio XI, derived from PALSAR images obtained on January 4 and February 19, 2011. Temporal evolution in the average velocity at each of the three profiles (A–B, C–D, and E–F) is shown in (b–d). (b) Temporal changes in the average frontal position and velocity across profile A–B in the northern tongue. (c) Temporal changes in the average frontal position and velocity across profile C–D in the southern tongue. (d) Temporal changes in the average velocity across profile E–F in the main upstream.

Figure 8: Temporal evolution of the frontal position at Glaciar Pio XI between 2002 and 2011. Background is a PALSAR-based scattering intensity image acquired on February 19, 2011.

Figure 9: Velocity increases observed at (a) Glaciar Upsala from January 2003 to January 2011, (b) Glaciar Jorge Montt from January 2003 to January 2011, and (c) Glaciar Occidental from January 2003 to January 2011.

Table 1: The processed SAR images

Sensor	Path (Track)	Frame	Acquisition date	Mode	A/D
PALSAR	129	6150	20100216	FBS	A
	129	6150,6160,6170,6180	20100519	FBD	A
	129	6150,6160,6170,6180	20100704	FBD	A
	129	6150,6160,6170,6180	20110104	FBS	A
	129	6150,6160,6170,6180	20110219	FBS	A
	130	6150,6160,6170,6180	20100605	FBD	A
	130	6150,6160,6170,6180	20100721	FBD	A
	130	6150	20101021	FBD	A
	130	6150	20110121	FBS	A
	410	4650	20070619	FBD	D
	410	4650	20070919	FBD	D
	410	4650	20071104	FBD	D
	410	4650	20071220	FBS	D
	411	4650	20070706	FBD	D
	411	4650	20071121	FBD	D
	411	4650	20080106	FBS	D
	414	4600,4620	20070826	FBD	D
	414	4600,4620	20071011	FBD	D
	414	4600,4620	20080111	FBS	D
	414	4600,4620	20080226	FBS	D
ASAR	153	4599,4617,4635	20021220	I2	D
	153	4599,4617,4635	20030228	I2	D
	153	4599,4617,4635	20030613	I2	D
	153	4599,4617,4635	20030718	I2	D
	153	4599,4617,4635	20030926	I2	D

(continued)

Sensor	Path (Track)	Frame	Acquisition date	Mode	A/D
	153	4599,4617,4635	20031205	I2	D
	153	4599,4617,4635	20040109	I2	D
	153	4599,4617,4635	20040910	I2	D
	153	4599,4617,4635	20050722	I2	D
	153	4599,4617,4635	20050826	I2	D
	153	4599,4617,4635	20080815	I2	D
	196	4599	20021223	I2	D
	196	4599	20030616	I2	D
	196	4599	20031208	I2	D
	196	4599	20040122	I2	D
	196	4599	20040322	I2	D
	196	4599	20040426	I2	D
	196	4599	20040531	I2	D
	196	4599	20040913	I2	D
	196	4599	20050620	I2	D
	196	4599	20050829	I2	D
	196	4599	20051003	I2	D
	196	4599	20070730	I2	D
	376	6147	20050703	I6	A
	376	6147	20050807	I6	A
	376	6147	20050911	I6	A
	382	4635	20030629	I2	D
	382	4635	20030803	I2	D
	382	4635	20040125	I2	D
	382	4635	20040229	I2	D
	382	4635	20040404	I2	D

(continued)

Sensor	Path (Track)	Frame	Acquisition date	Mode	A/D
	382	4635	20040509	I2	D
	382	4635	20040613	I2	D
	425	4599,4617	20030108	I2	D
	425	4599,4617	20030212	I2	D
	425	4599,4617	20030423	I2	D
	425	4599,4617	20030702	I2	D
	425	4599,4617	20031015	I2	D
	425	4599,4617	20040407	I2	D
	425	4599,4617	20040512	I2	D
	425	4599,4617	20040825	I2	D
	425	4599,4617	20080903	I2	D

Table 2: The imaging angles and offsets as a function of 3-D displacements

Sensor	Mode (A/D)	H (deg.)	I (deg.)	U_{ra}	U_{az}
PALSAR	A	-20	39	$0.59U_e+0.22U_n-0.78U_z$	$-0.34U_e+0.94U_n$
PALSAR	D	-159	39	$-0.59U_e+0.22U_n-0.78U_z$	$-0.36U_e-0.93U_n$
ASAR	IS6 (A)	-22	41	$0.61U_e+0.25U_n-0.75U_z$	$-0.37U_e+0.93U_n$
ASAR	IS2 (D)	-162	23	$-0.37U_e+0.12U_n-0.92U_z$	$-0.31U_e-0.95U_n$

Supplementary material for “Surface Velocities and Ice-Front Positions of Eight Major Glaciers in the Southern Patagonian Ice Field, South America, from 2003 to 2011” by Minami Muto and Masato Furuya

We examined the surface velocity and frontal position evolution at eight glaciers in South Patagonian Ice Field, and showed in the main text the results of four glaciers that indicated significant temporal changes. With the exceptions of Glacier Upsala and the site C at Glacier Jorge Montt, we first selected five velocity profiles at nearly the same location across the flow direction of each glacier, and then derived an average and standard deviation of them as a measurement error.

The supplementary figures show temporal changes in the average frontal position and average velocities for the four glaciers not shown in the main text. In addition, the temporal changes of each velocity profile and standard deviation are also shown at the seven glaciers with the exception of Glacier Upsala.

Glacier Perito Moreno

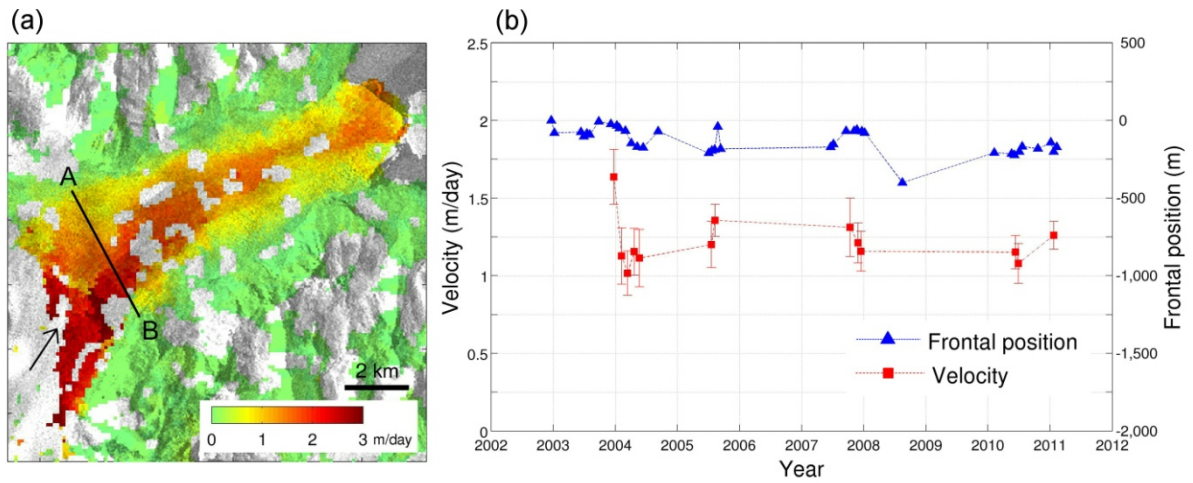


Figure S1: (a) Spatial distribution of surface flow velocities at Glacier Perito Moreno, derived from ASAR images obtained on July 3 and August 7, 2005. (b) Temporal changes in the average frontal position and velocities at profile A-B.

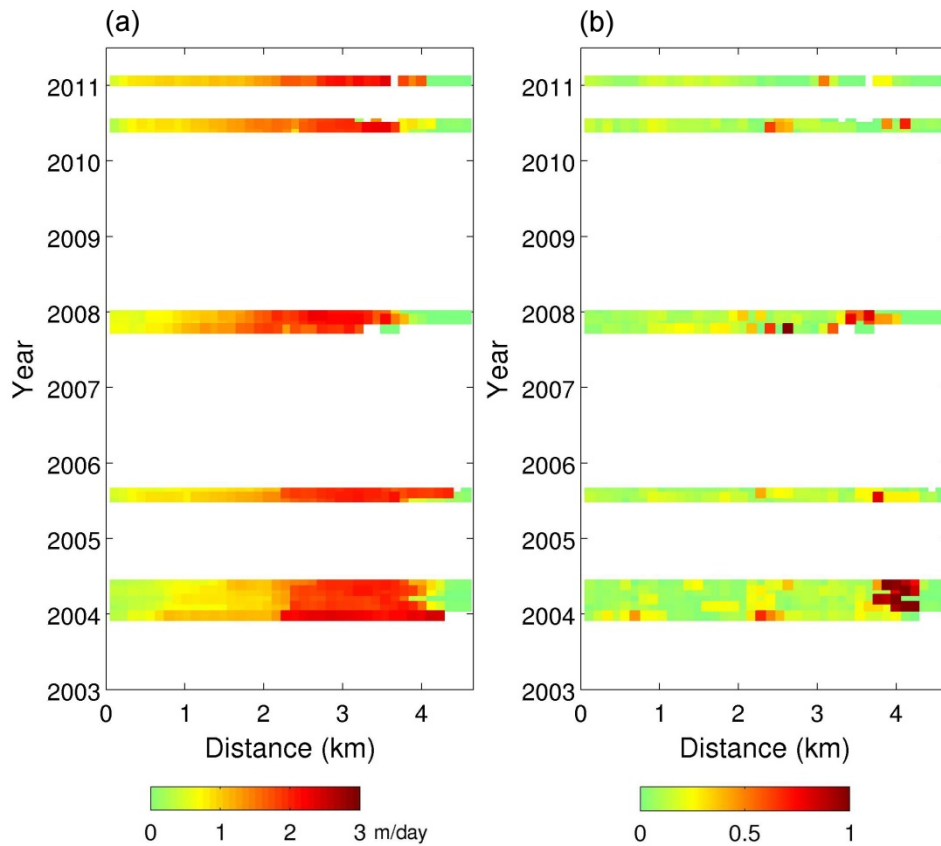


Figure S2: (a) Temporal evolution of the velocity profile A-B in Figure S1. (b) Estimated errors of the velocity profile at each epoch.

Glacier O'Higgins

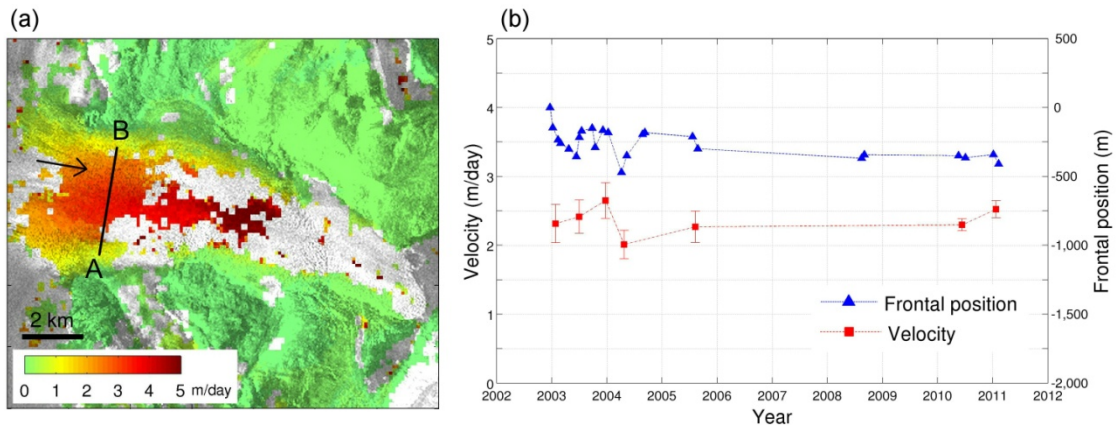


Figure S3: (a) Spatial distribution of surface flow velocities at Glacier O'Higgins, derived from PALSAR images obtained on January 4 and February 19, 2011. (b) Temporal changes in the average frontal position and velocities at profile A-B.

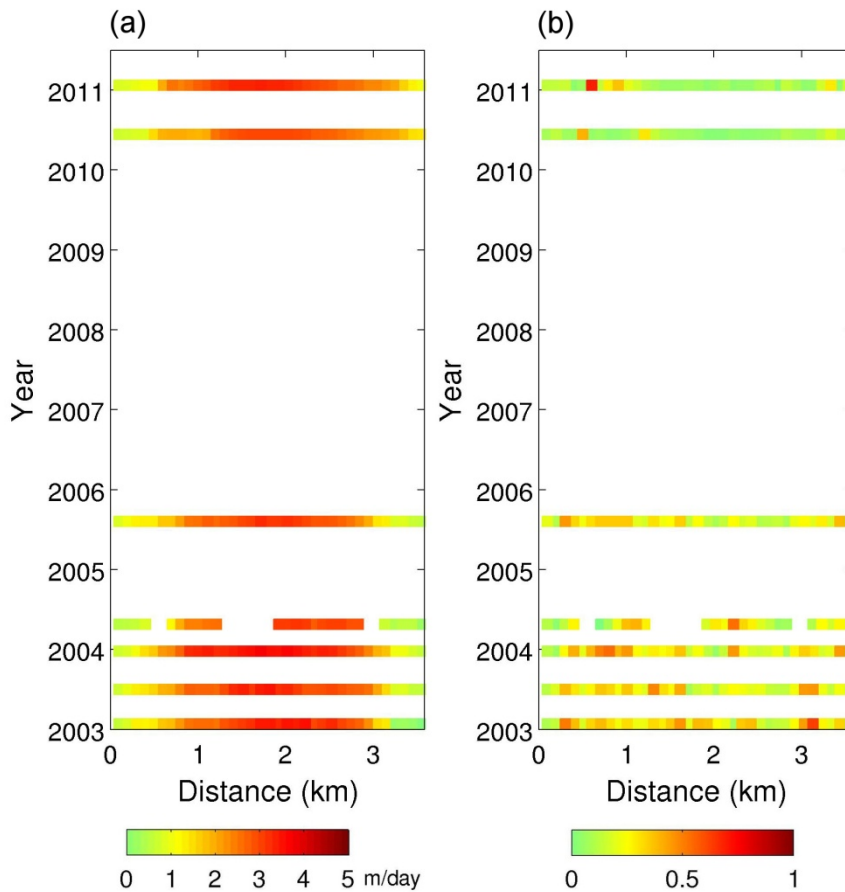


Figure S4: (a) Temporal evolution of the velocity profile A-B in Figure S3. (b) Estimated errors of the velocity profile at each epoch.

Glacier Viedma

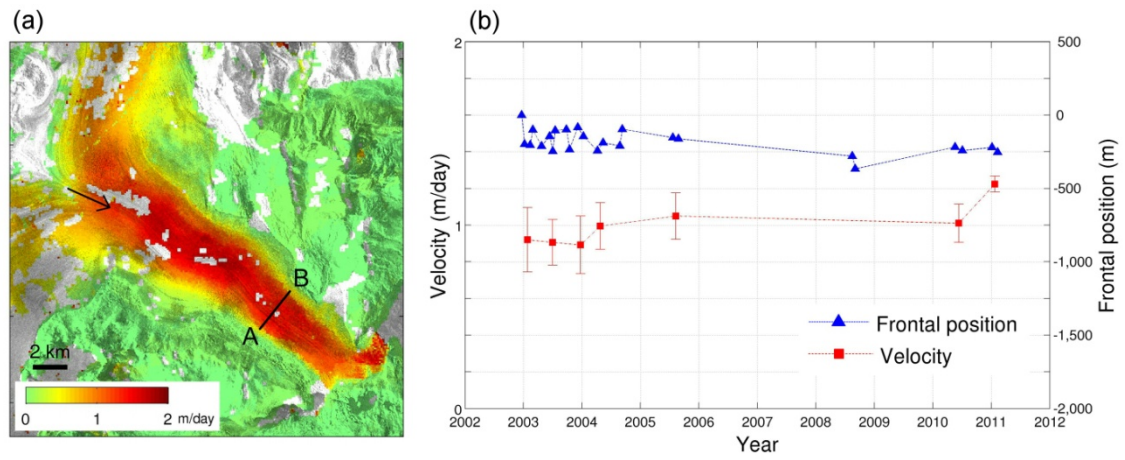


Figure S5: (a) Spatial distribution of surface flow velocities at Glacier Viedma, derived from PALSAR images obtained on January 4 and February 19, 2011. (b) Temporal changes in the average frontal position and velocities at profile A-B.

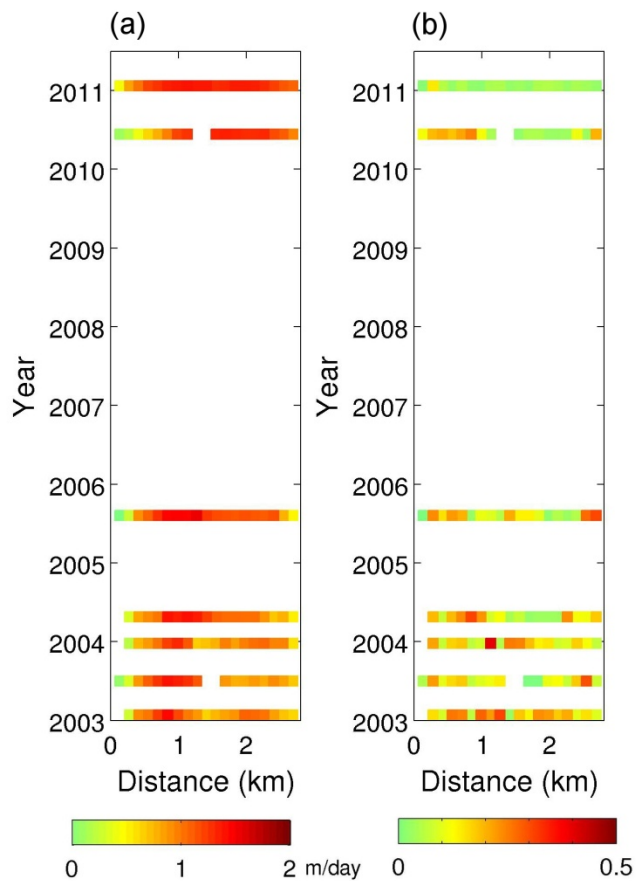


Figure S6: (a) Temporal evolution of the velocity profile A-B in Figure S5. (b) Estimated errors of the velocity profile at each epoch.

Glacier Grey

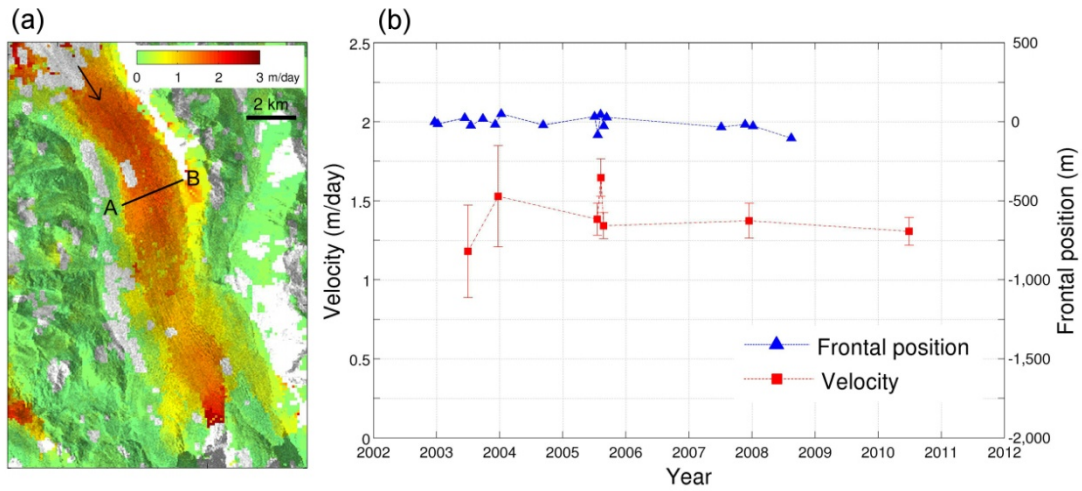


Figure S7: (a) Spatial distribution of surface flow velocities at Glacier Grey, derived from ASAR images obtained on July 3 and August 7, 2005. (b) Temporal changes in the average frontal position and velocities at profile A-B.

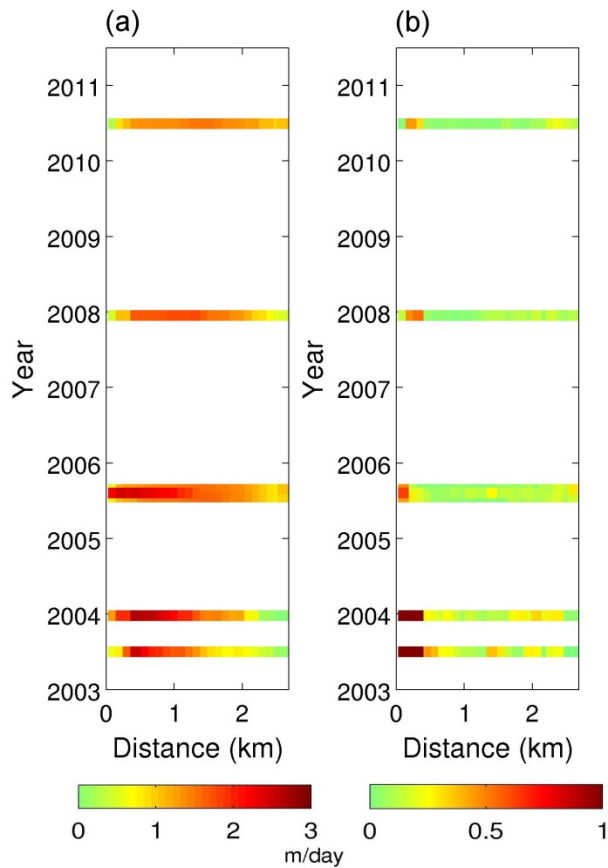


Figure S8: (a) Temporal evolution of the velocity profile A-B in Figure S7. (b) Estimated errors of the velocity profile at each epoch.

Glacier Jorge Montt

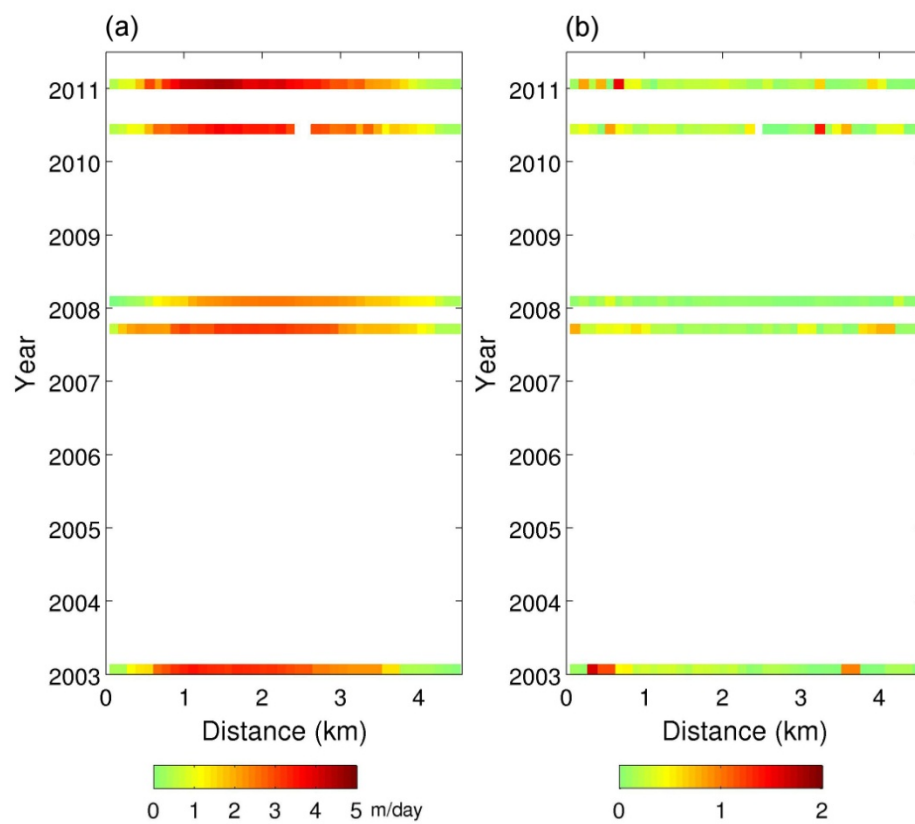


Figure S9: (a) Temporal evolution of the velocity profile A-B in Figure 4 in the main text. (b) Estimated errors of the velocity profile at each epoch.

Glacier Occidental

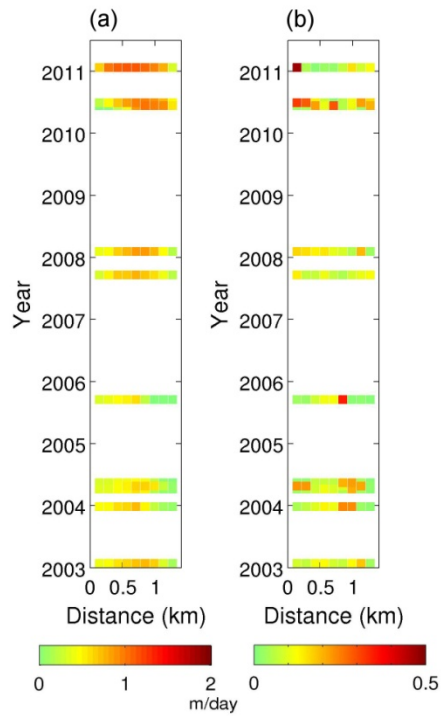


Figure S10: (a) Temporal evolution of the velocity profile A-B in Figure 6 in the main text. (b) Estimated errors of the velocity profile at each epoch.

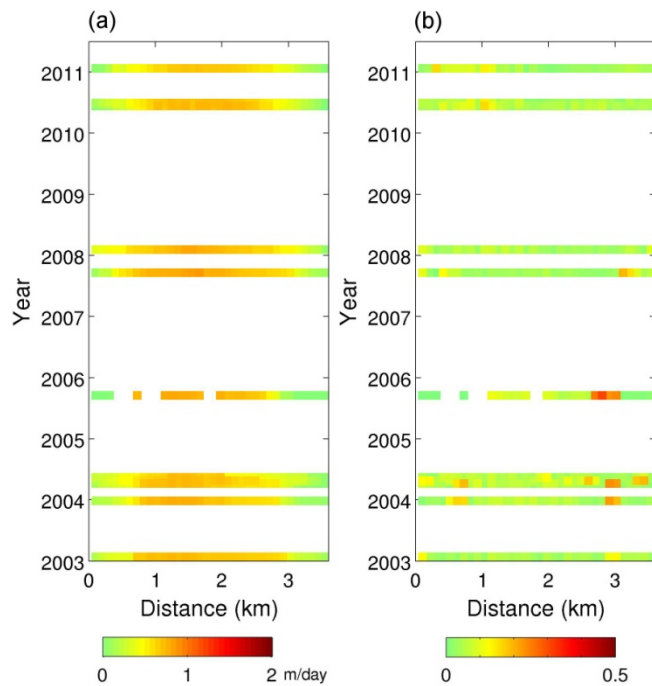


Figure S11: (a) Temporal evolution of the velocity profile C-D in Figure 6 in the main text. (b) Estimated errors of the velocity profile at each epoch.

Glacier PioXI

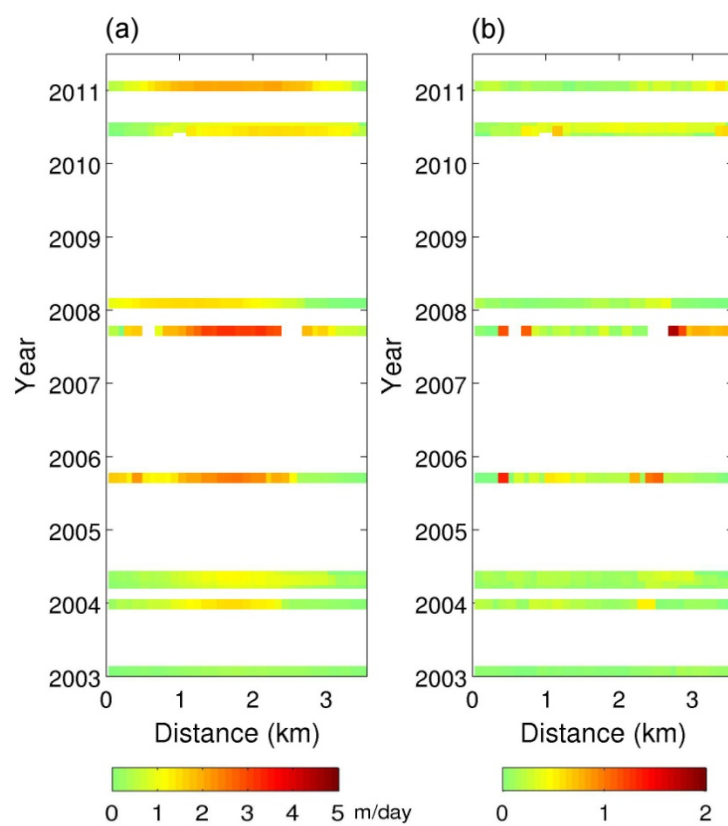


Figure S12: (a) Temporal evolution of the velocity profile A-B in Figure 7 in the main text. (b) Estimated errors of the velocity profile at each epoch.

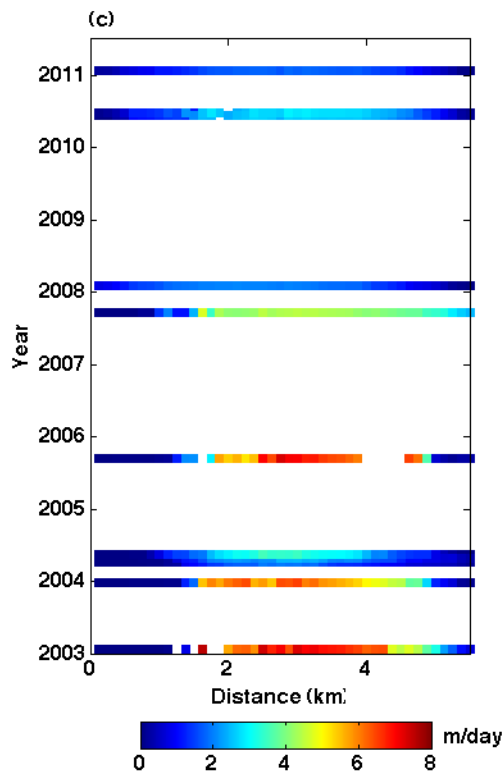
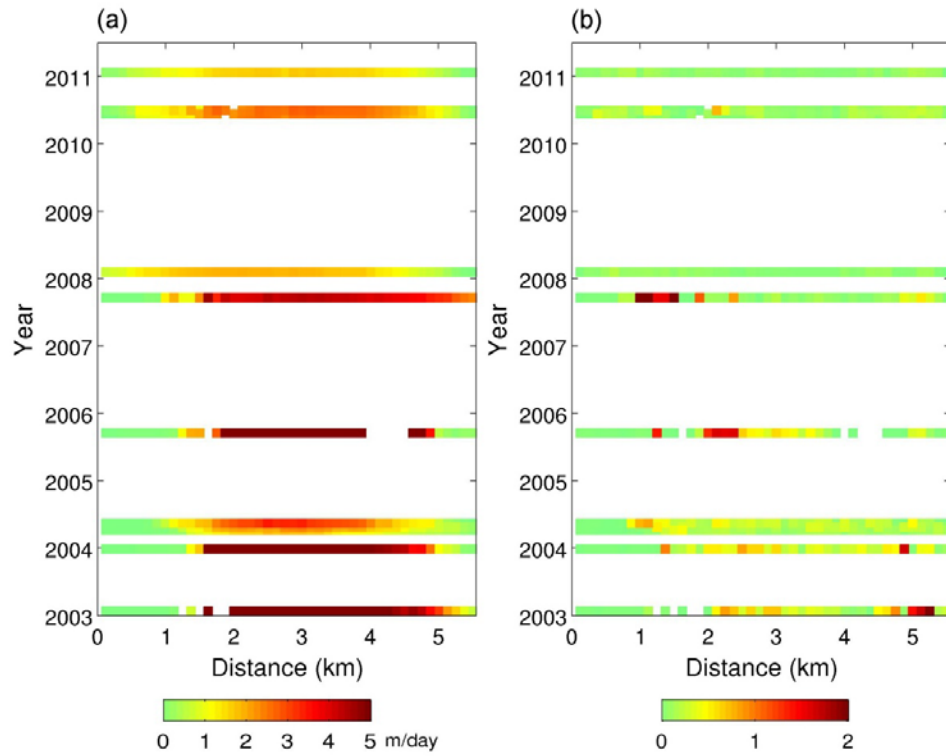


Figure S13: (a) Temporal evolution of the velocity profile C-D in Figure 7 in the main text. The velocities greater than 5 m/day are saturated in the color scale; see also (c). (b) Estimated errors of the velocity profile at each epoch. (c) Same temporal evolution in (a), but with different color scale and velocity range.

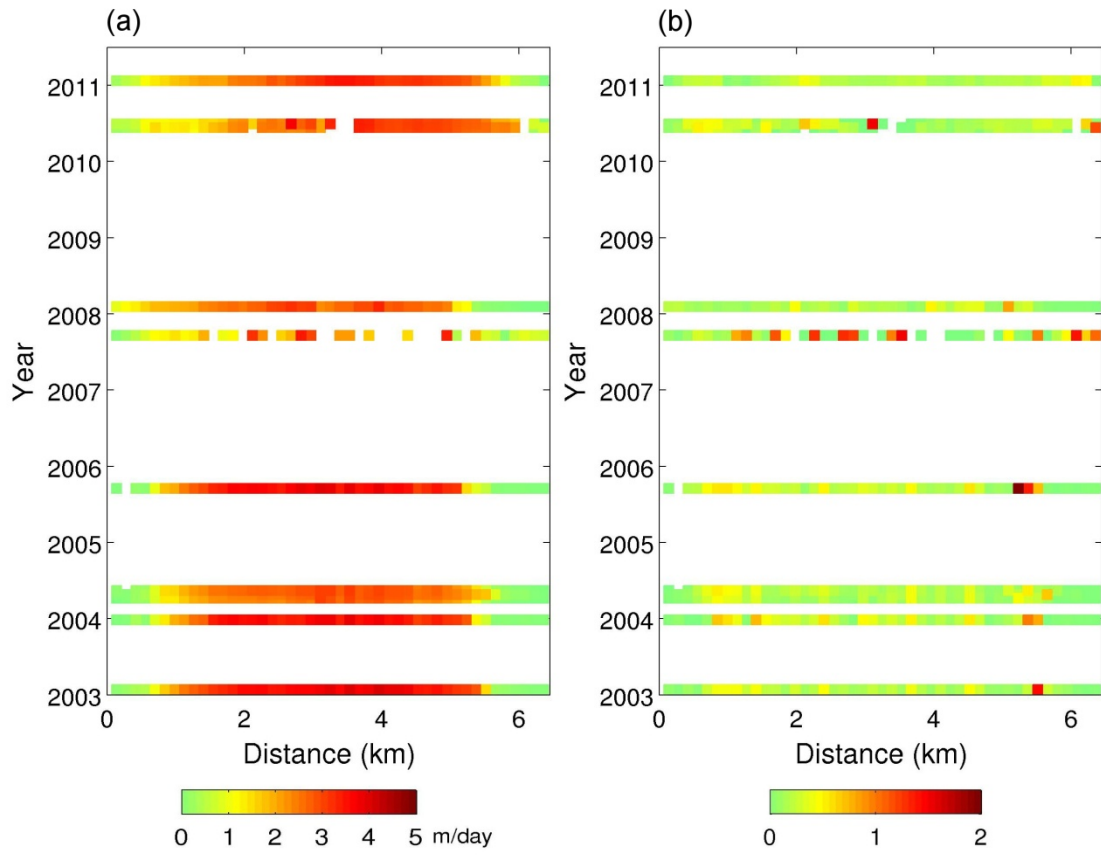
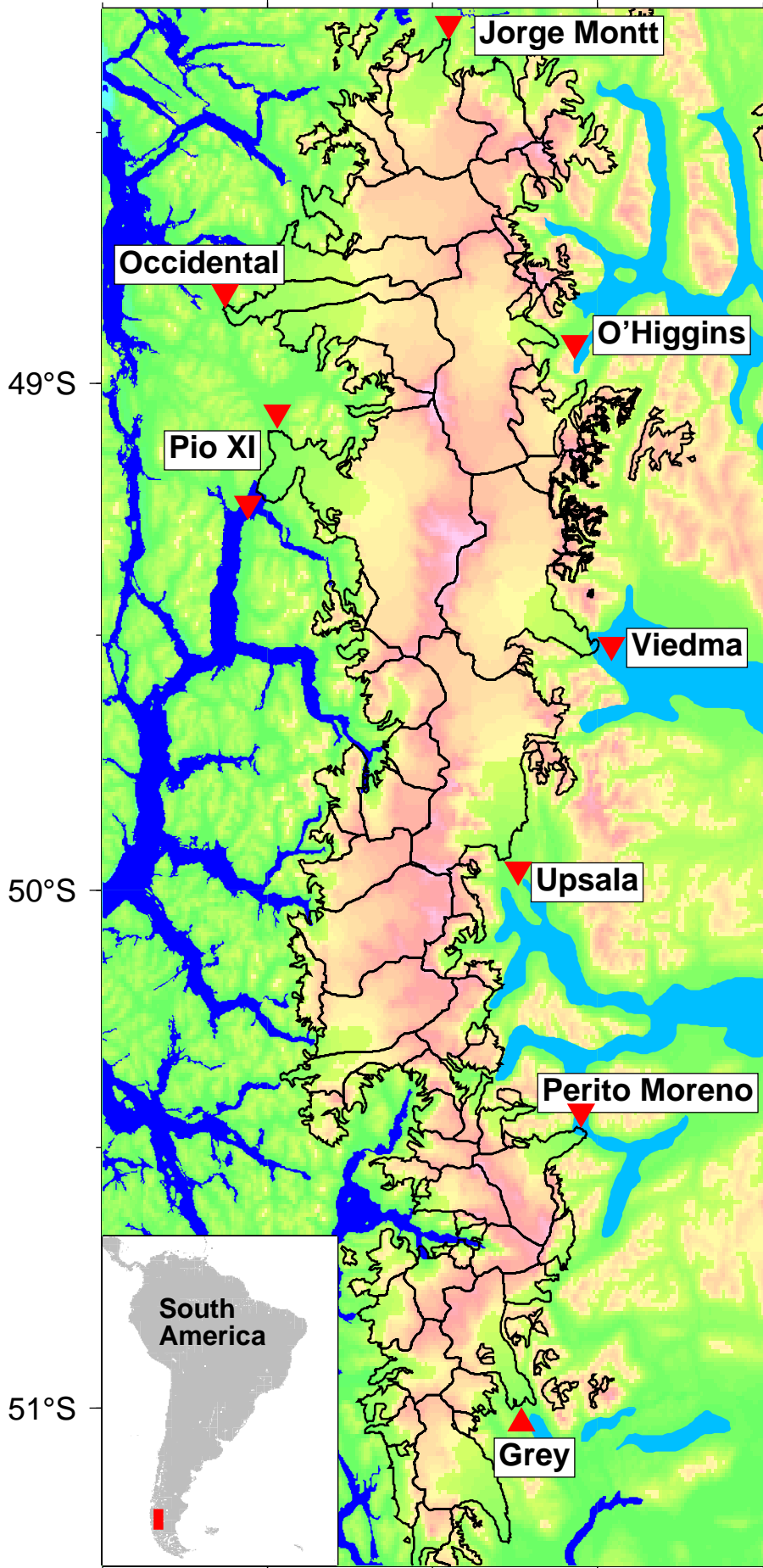


Figure S14: (a) Temporal evolution of the velocity profile E-F in Figure 7 in the main text. (b) Estimated errors of the velocity profile at each epoch.

74°W

73°W



49°S

50°S

51°S

Occidental

Pio XI

Jorge Montt

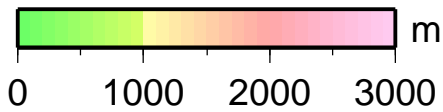
O'Higgins

Viedma

Upsala

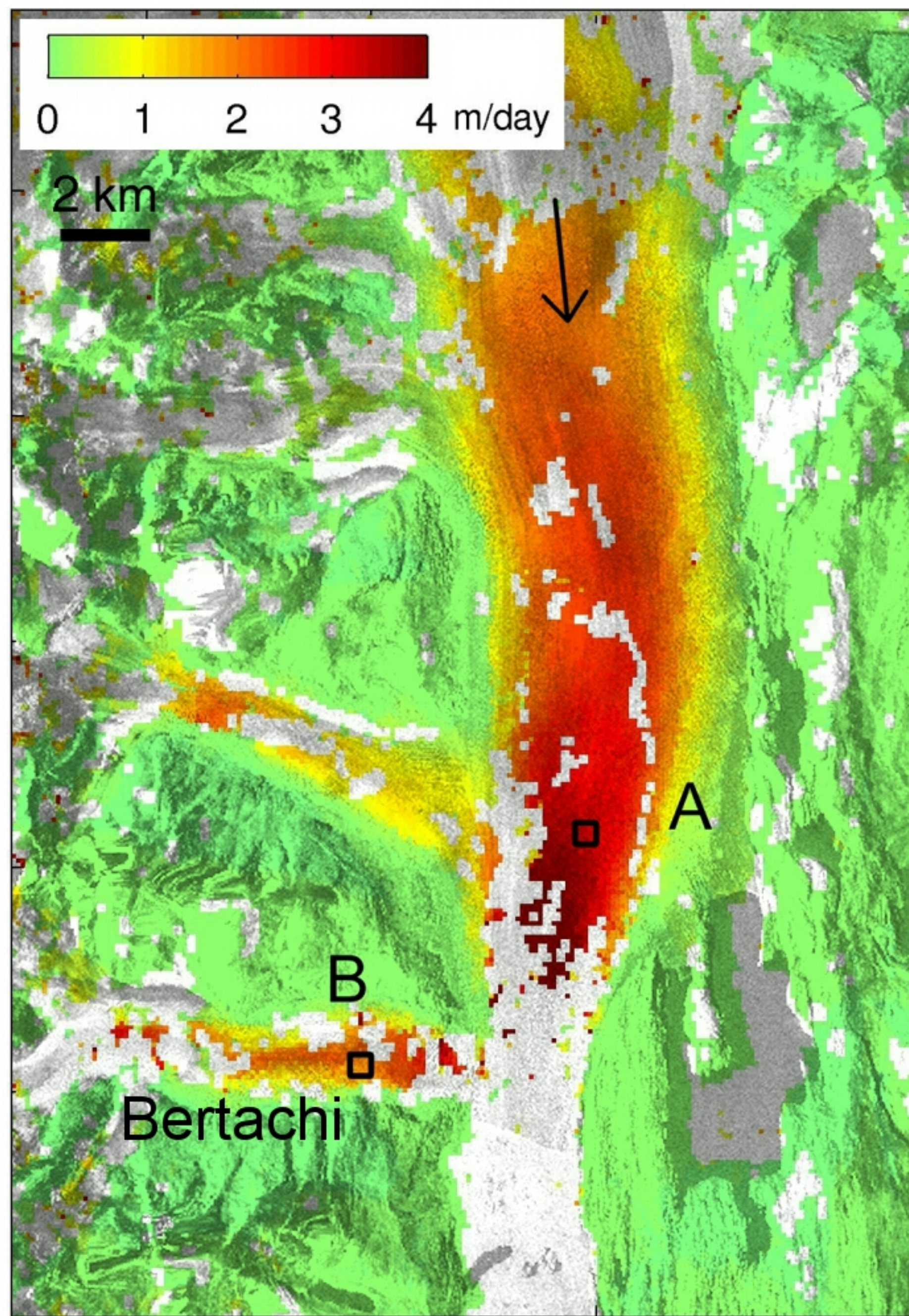
Perito Moreno

Grey

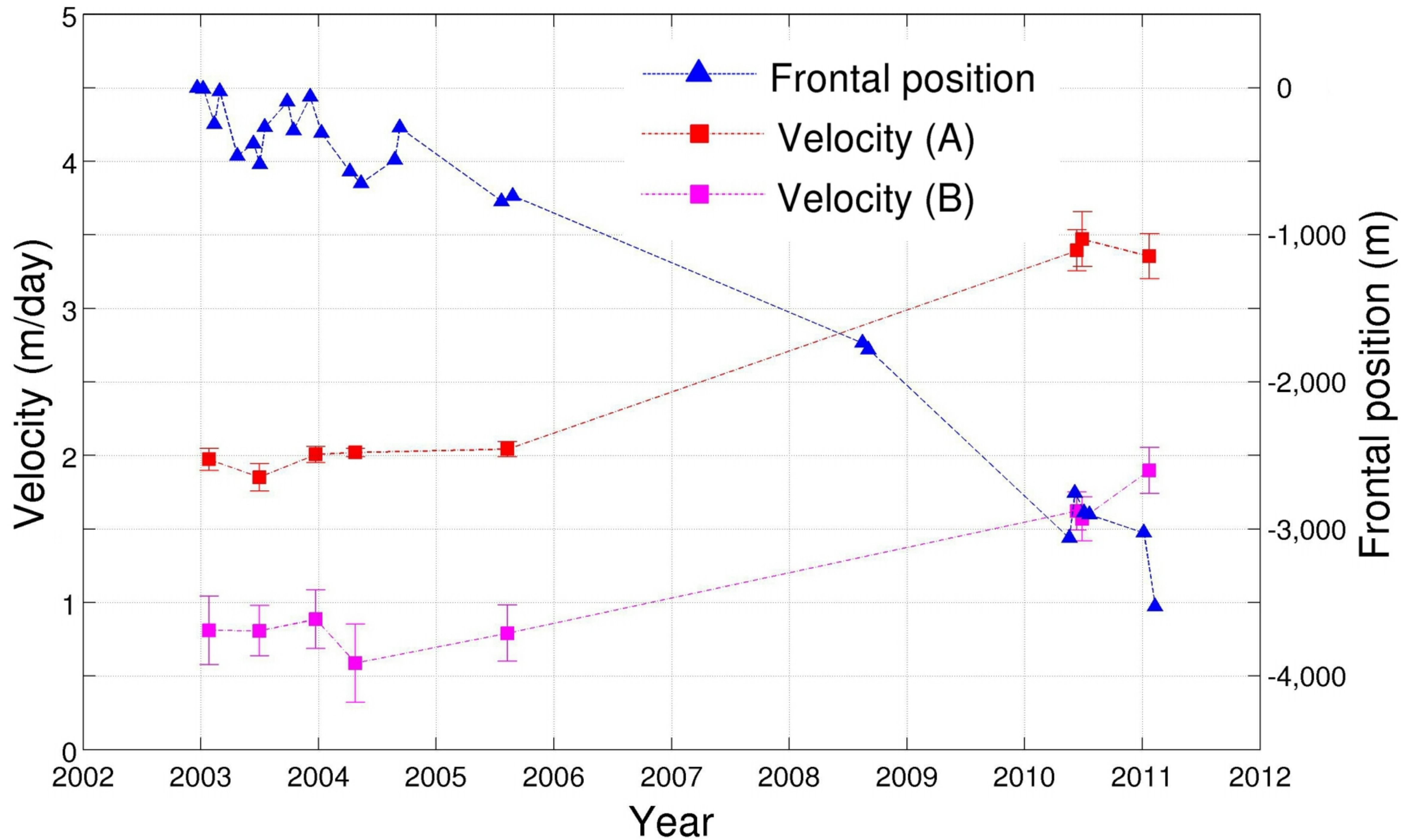


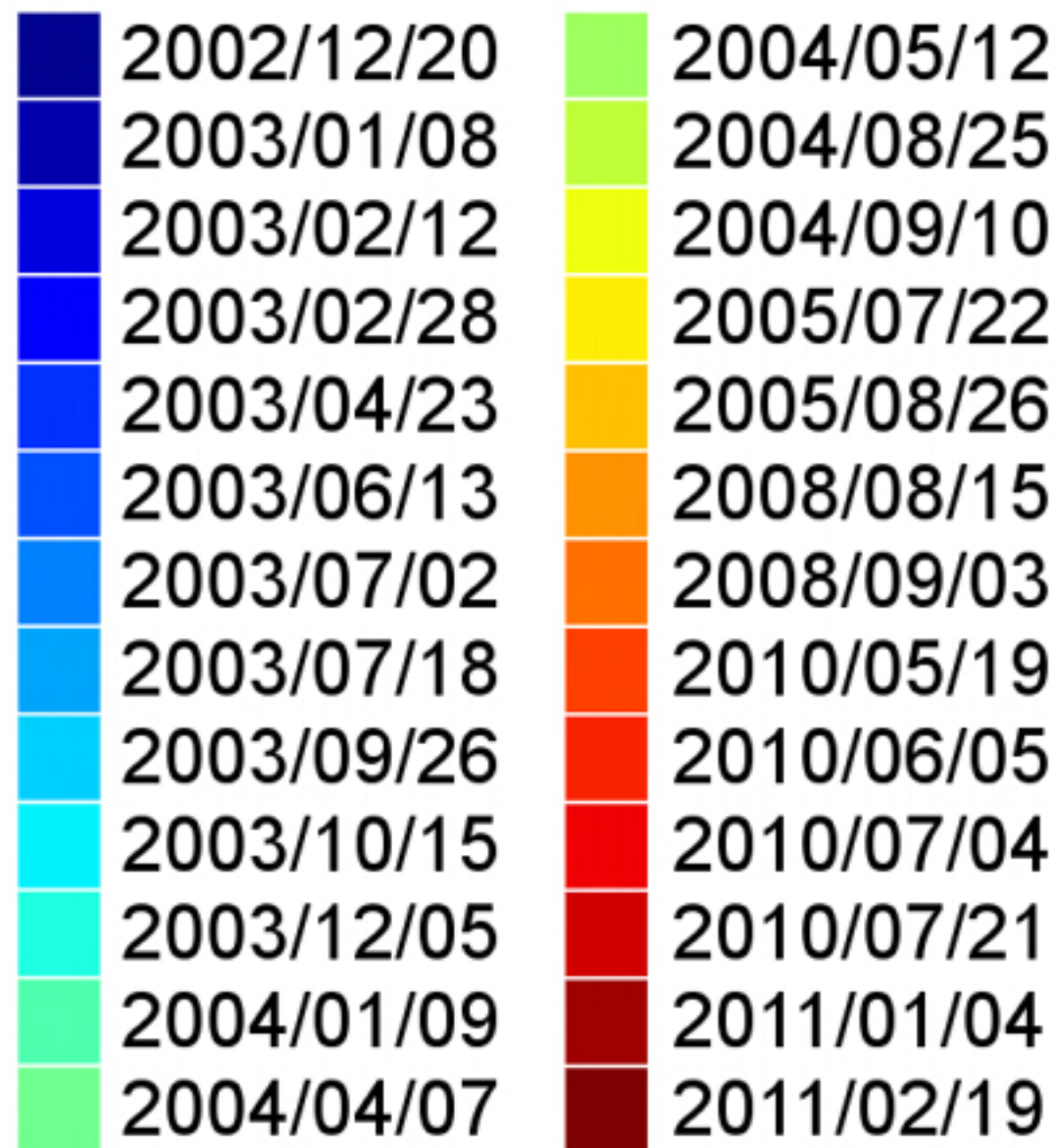
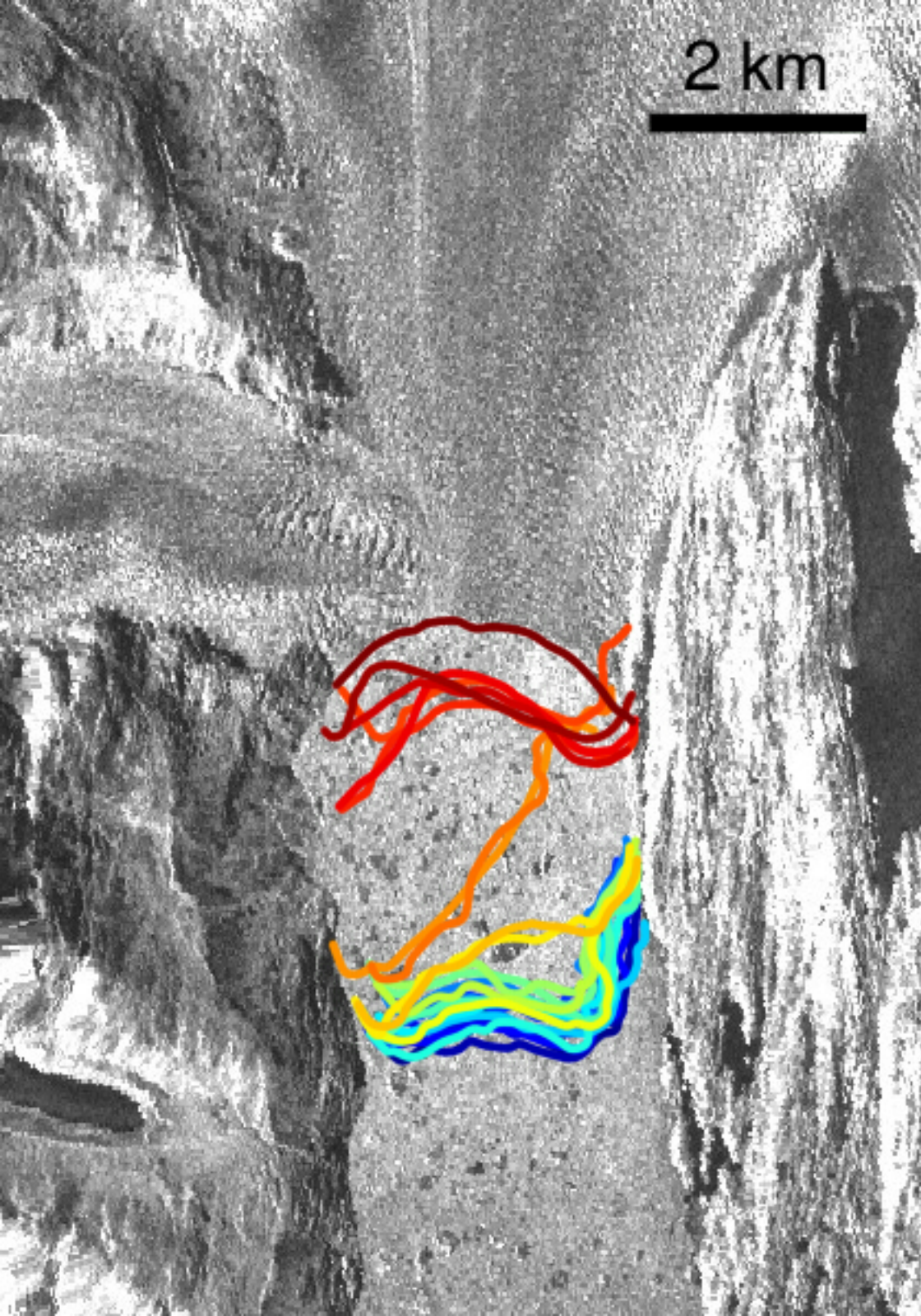
m

(a)

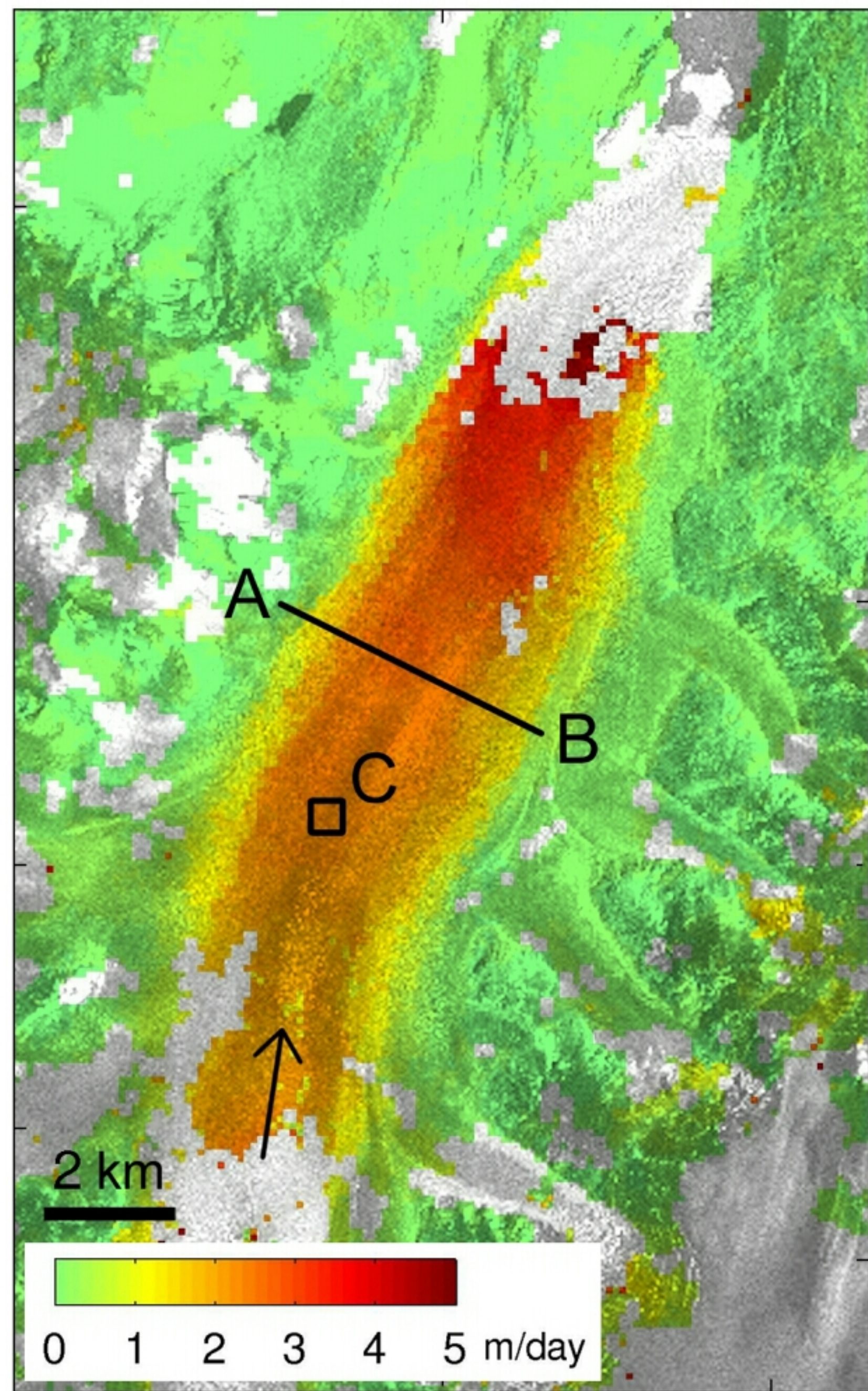


(b)

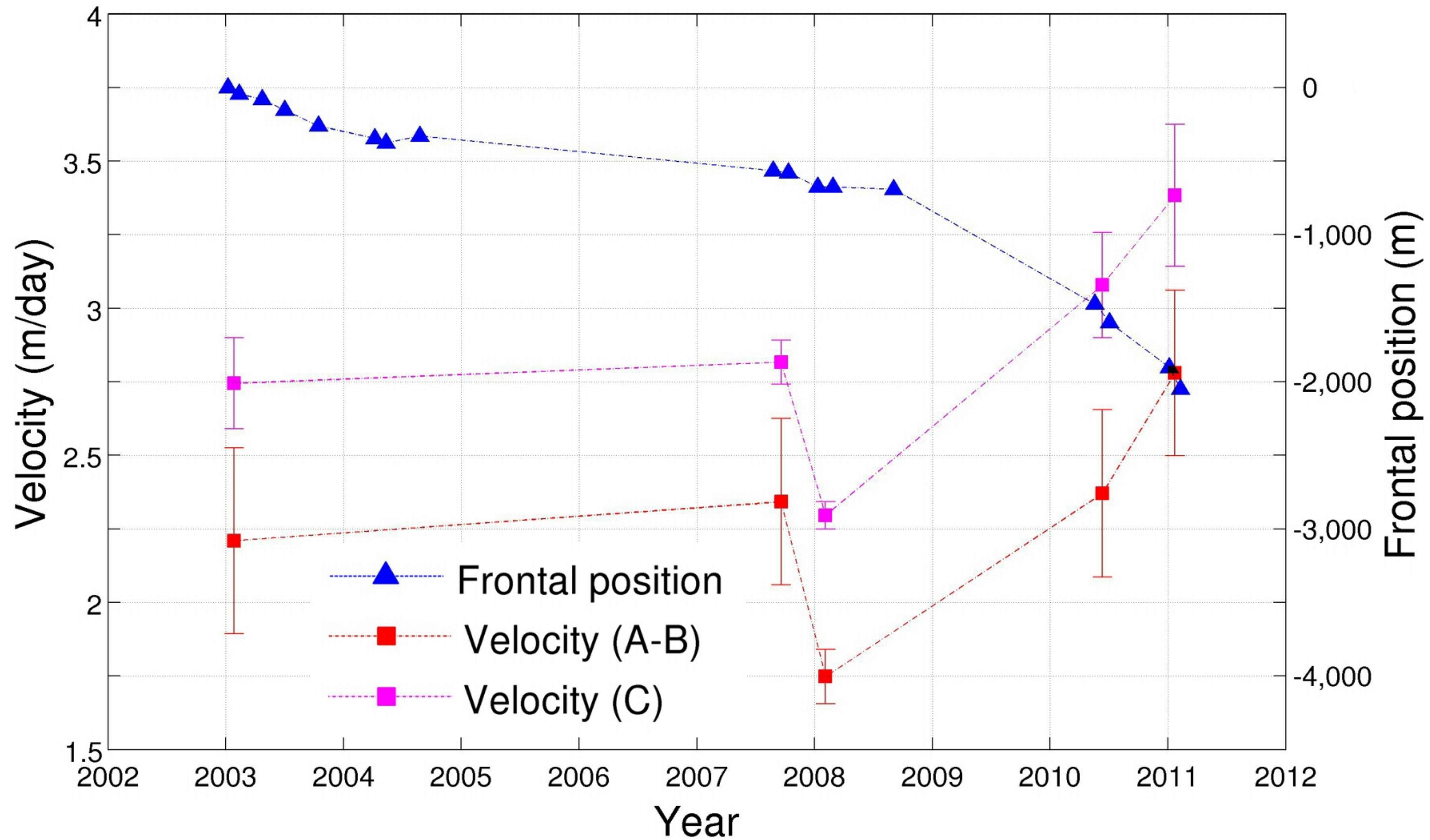


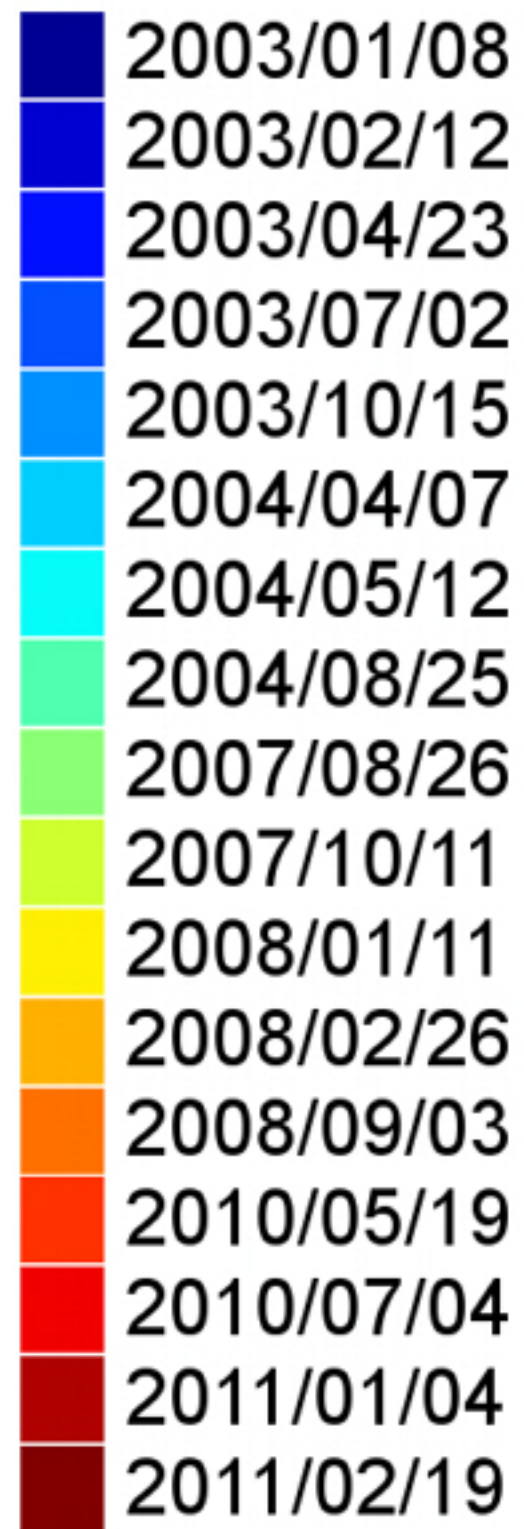
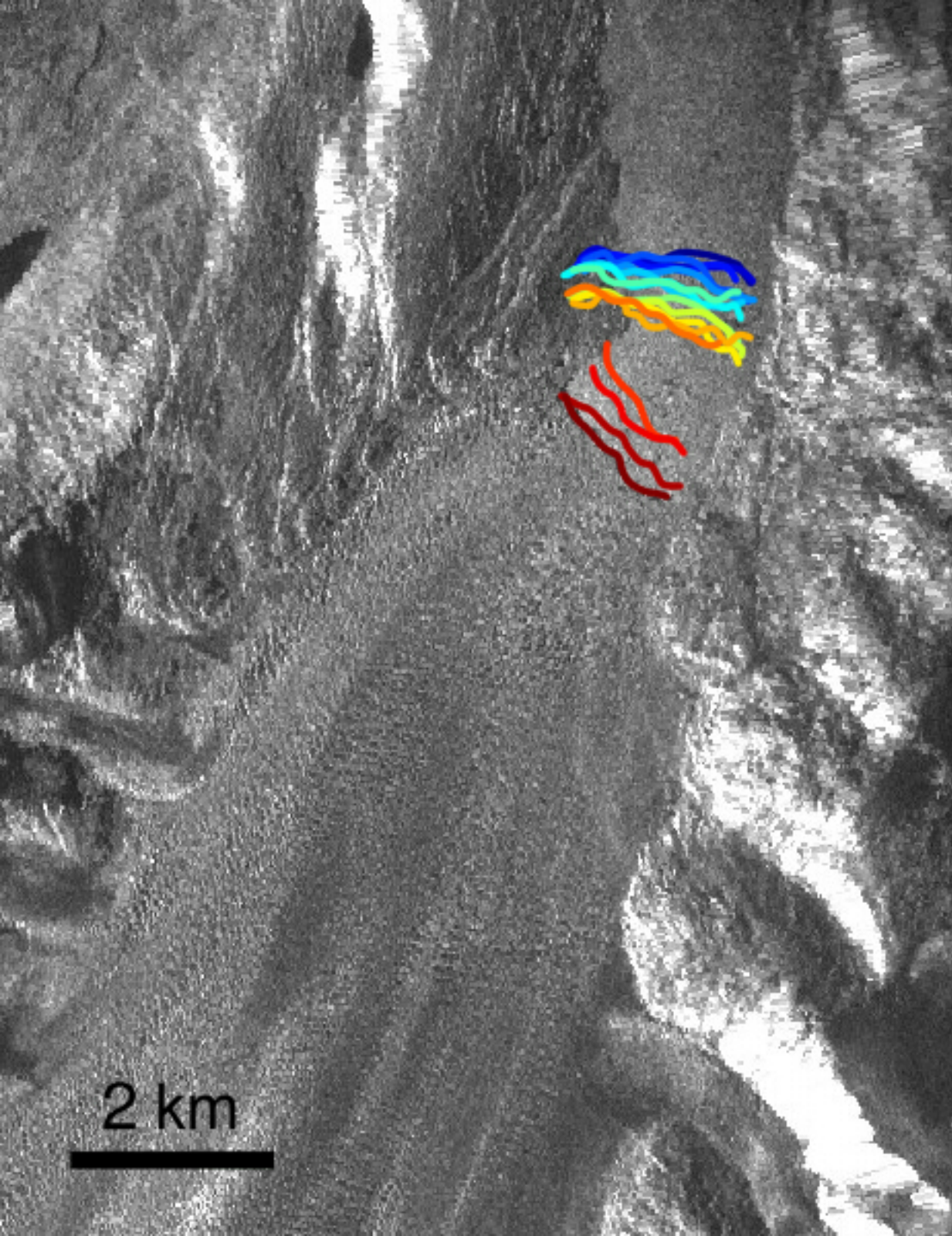


(a)

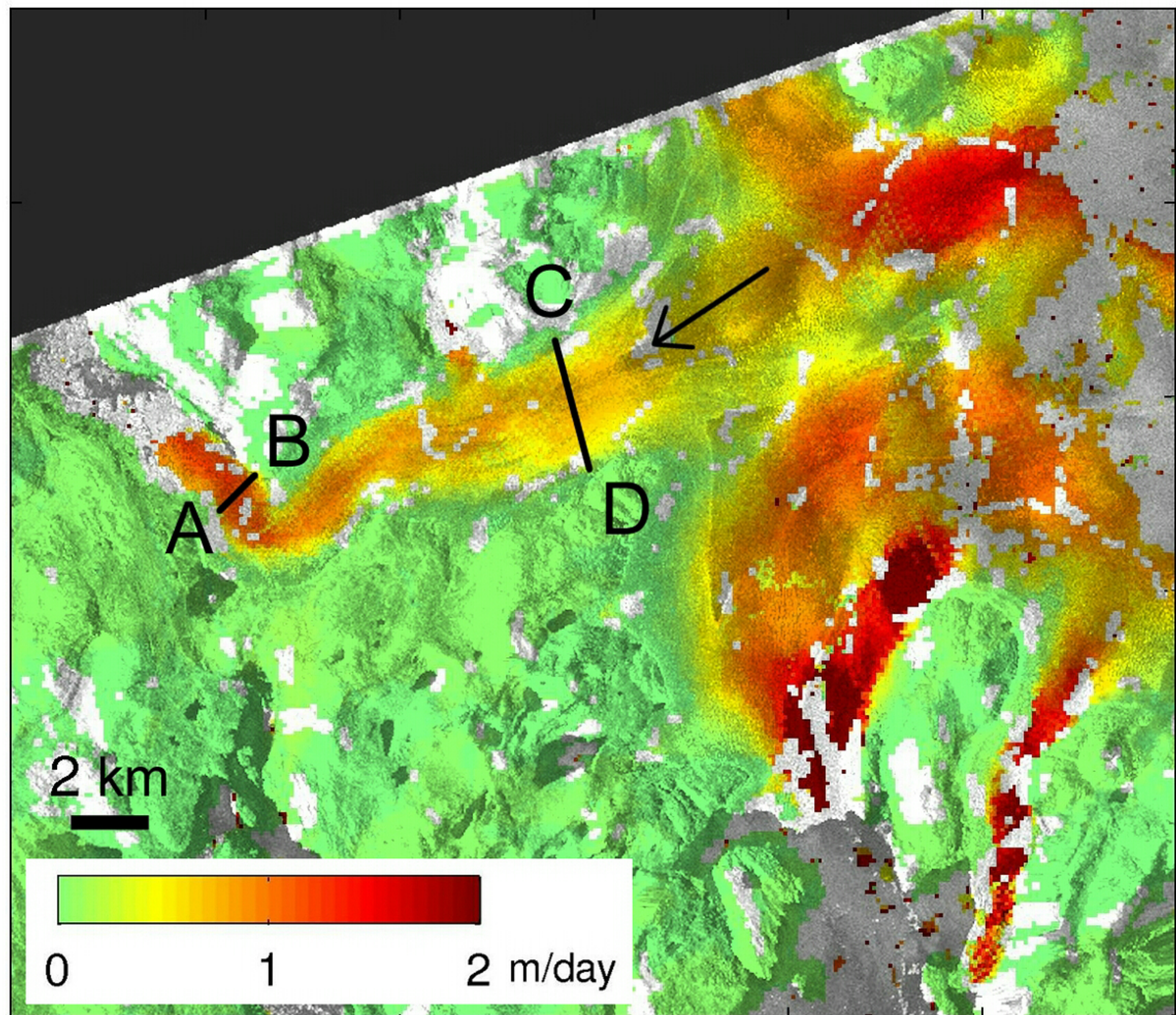


(b)

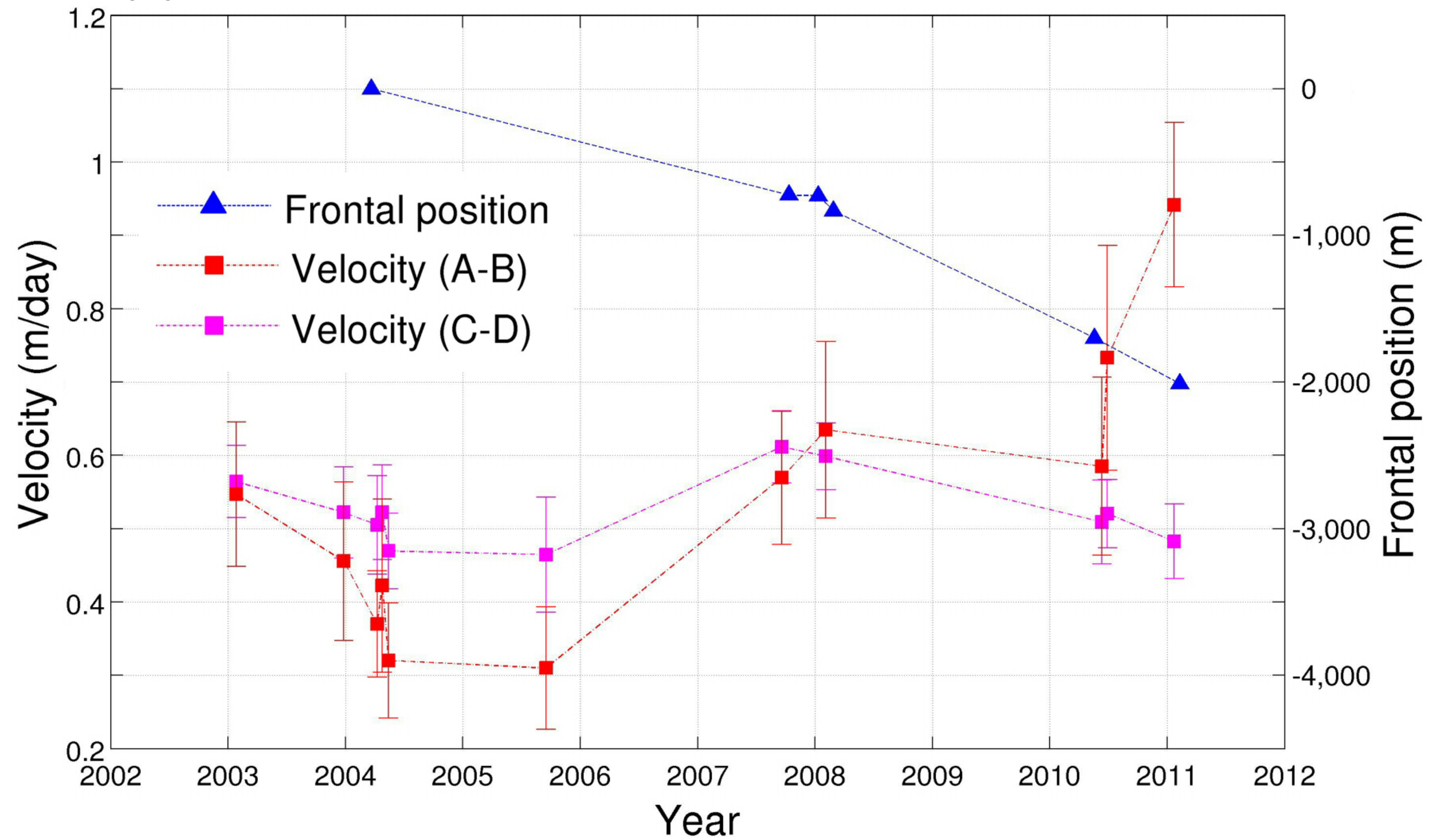




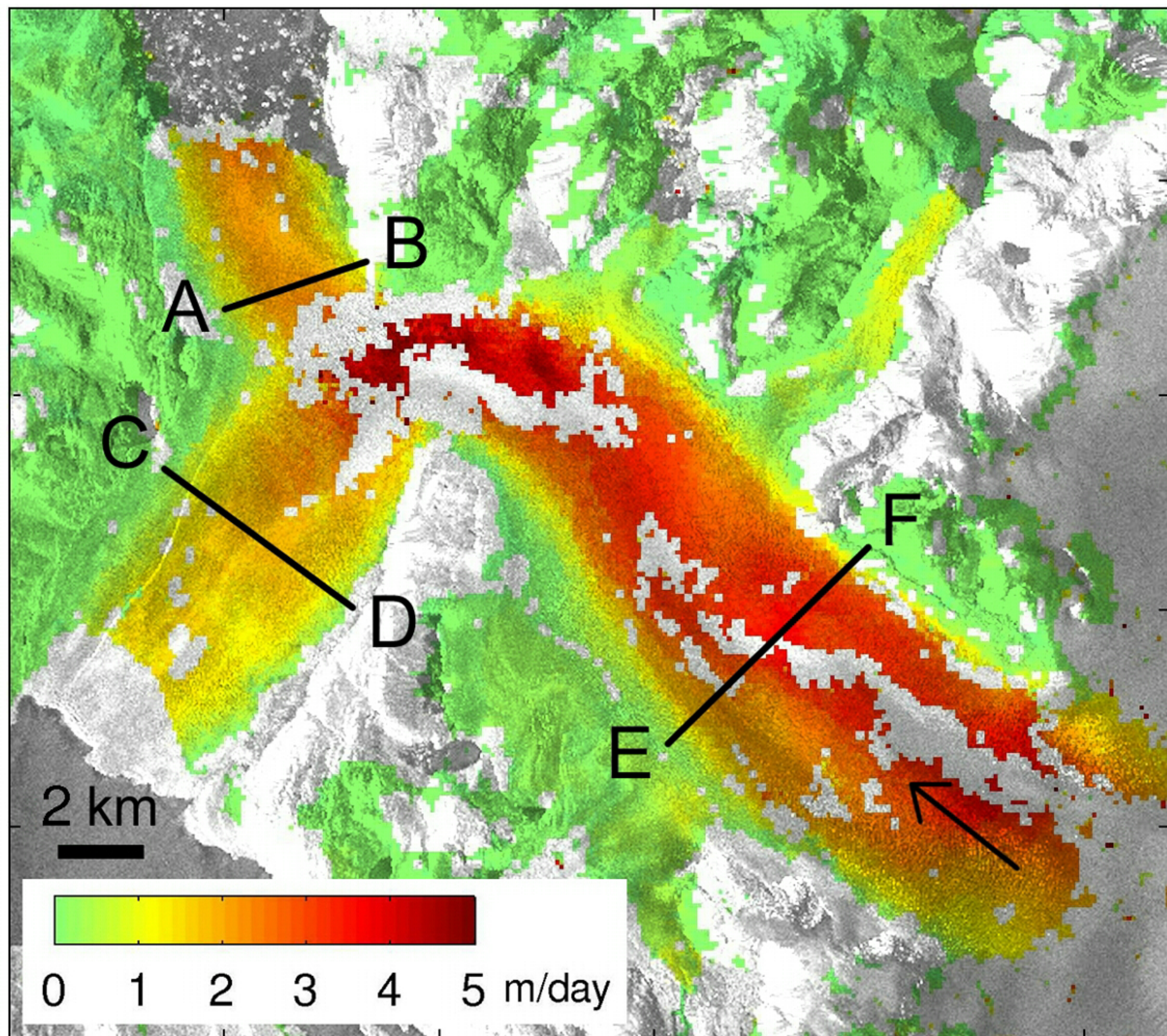
(a)



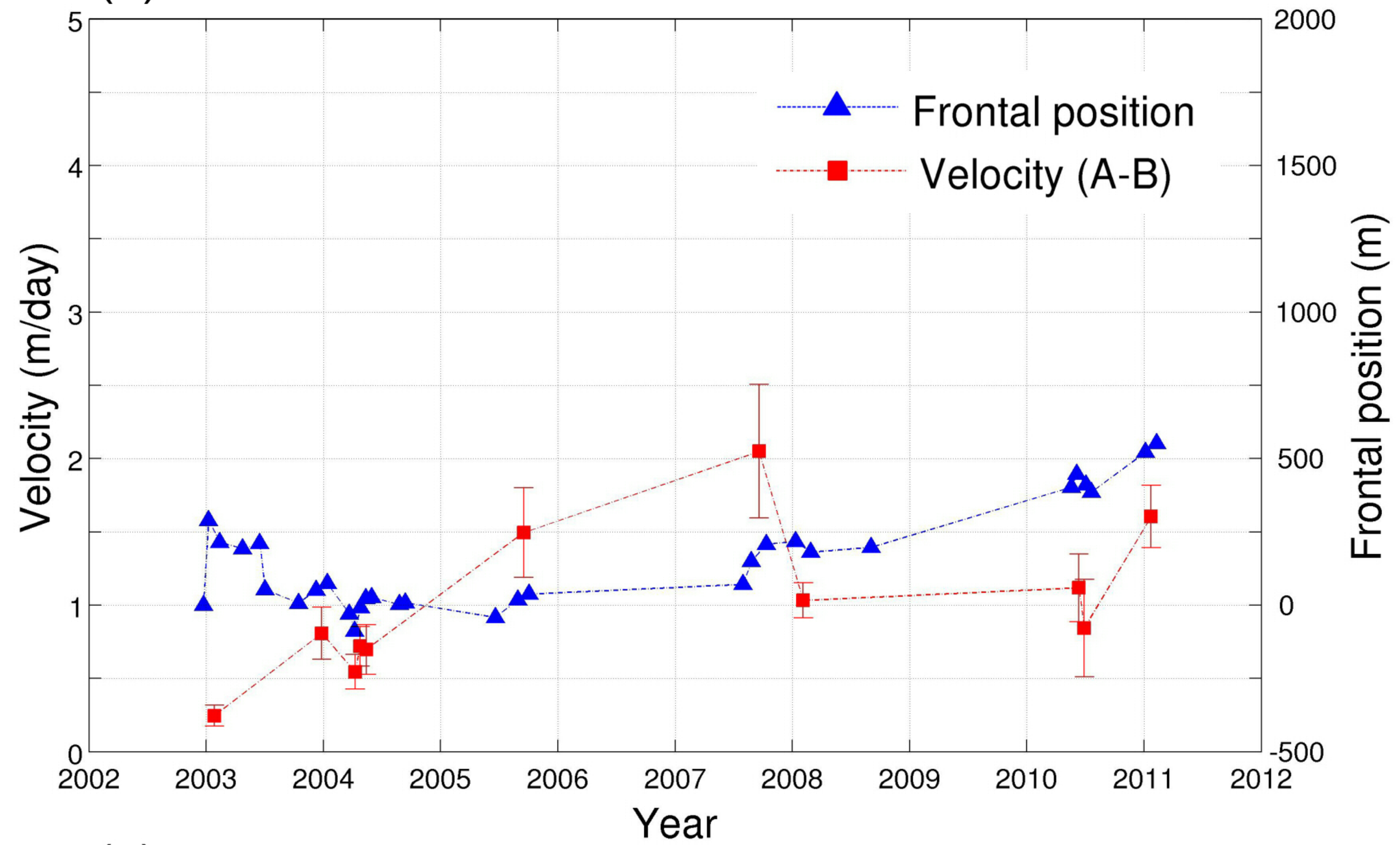
(b)



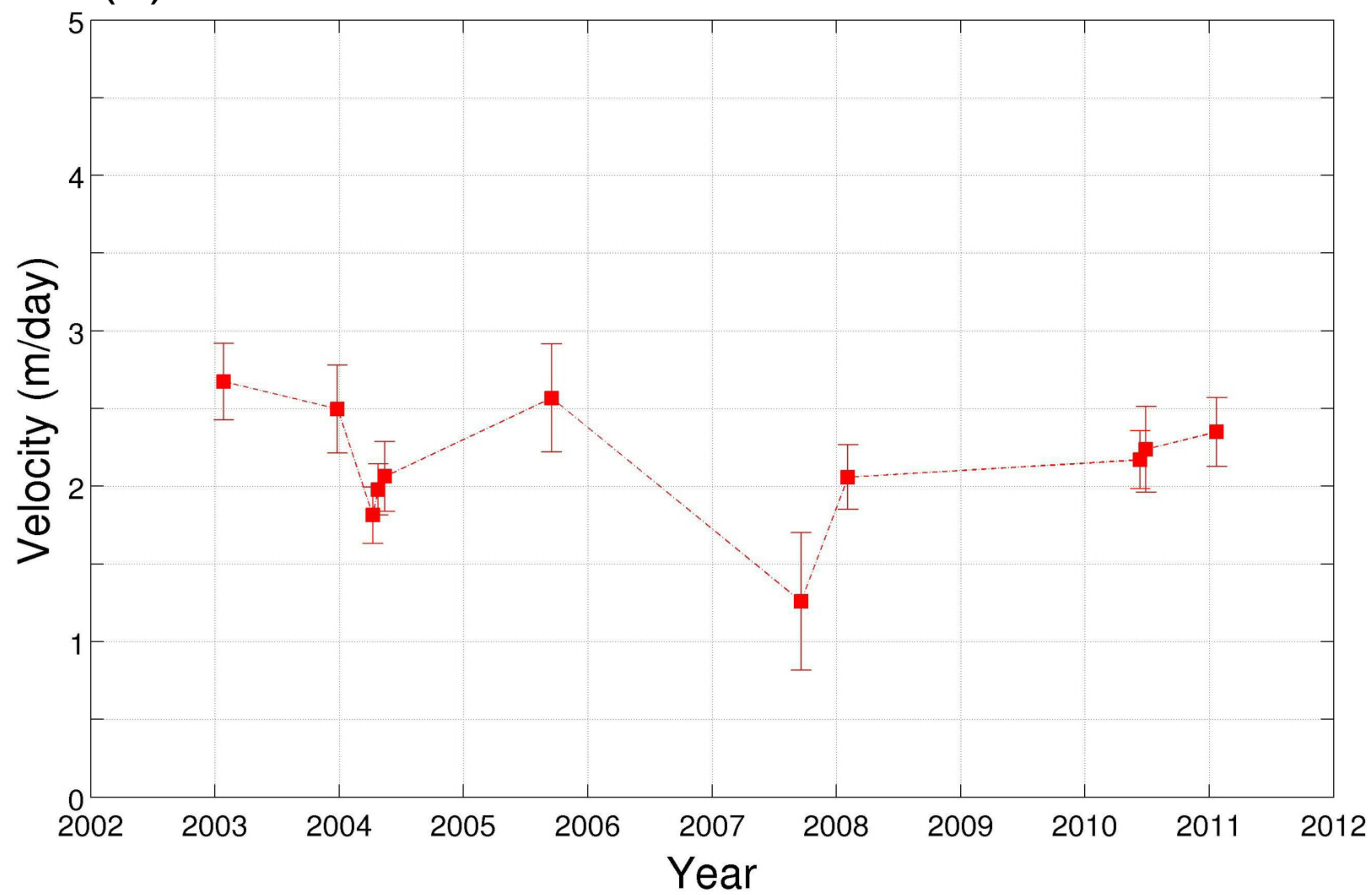
(a)



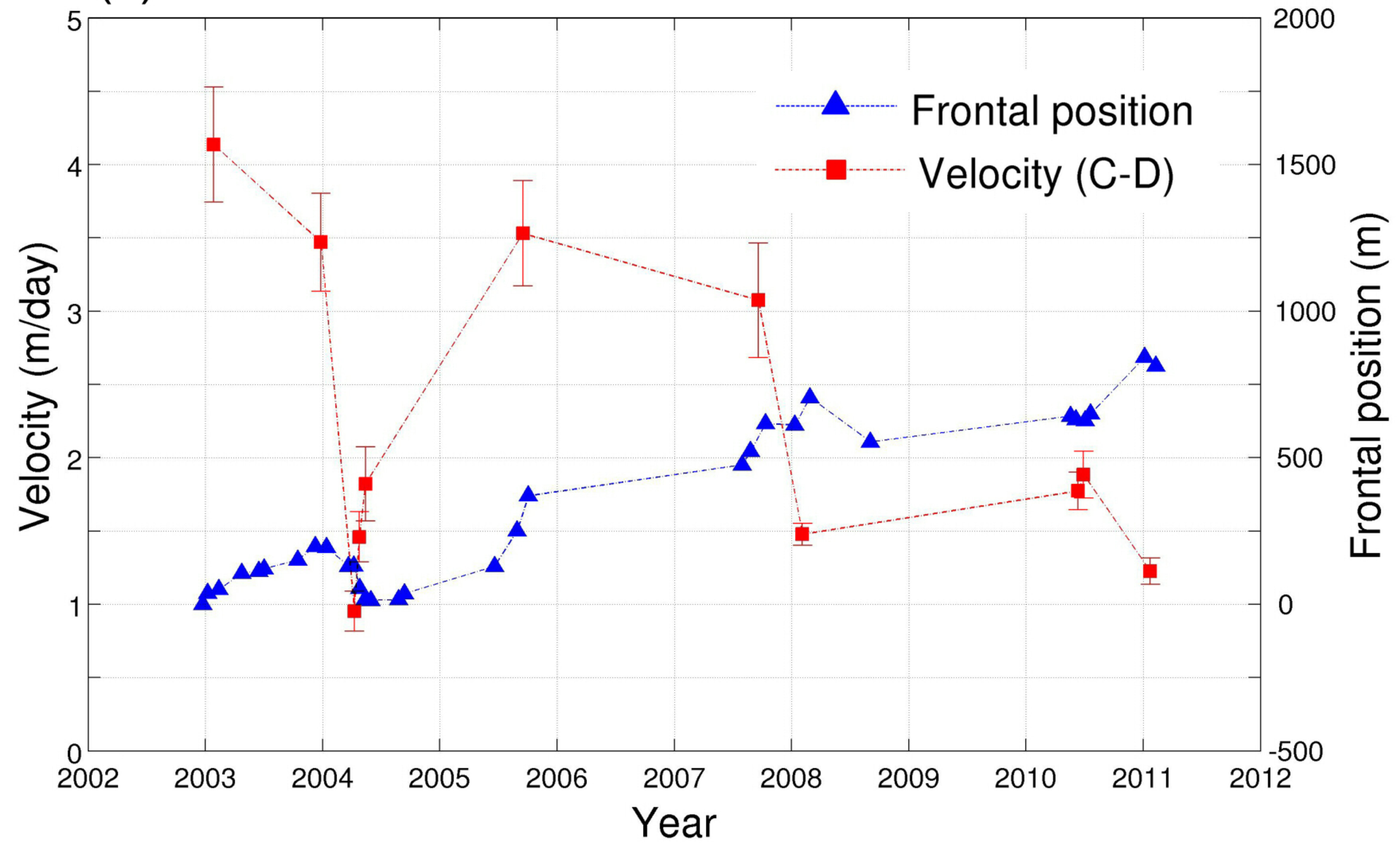
(b)

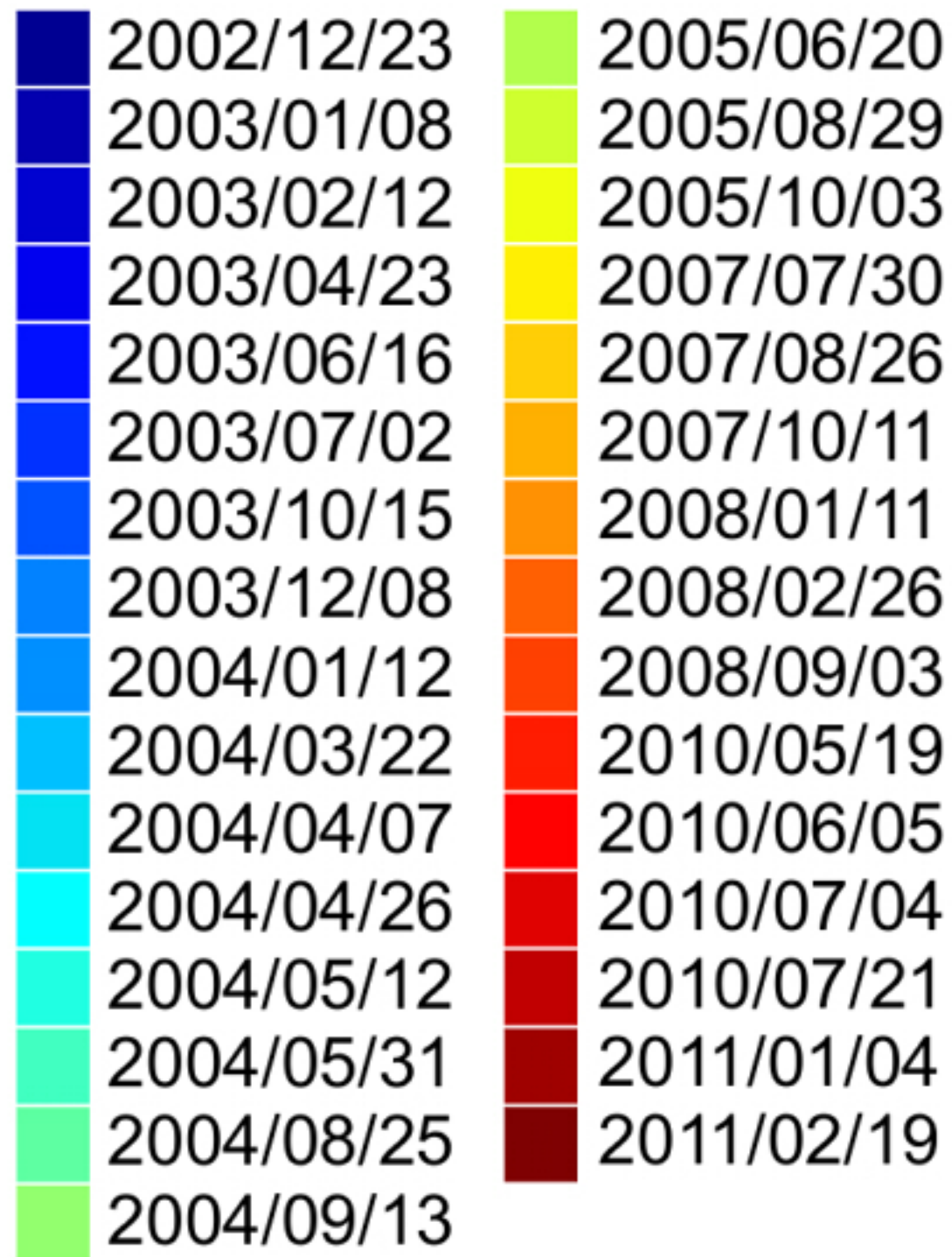
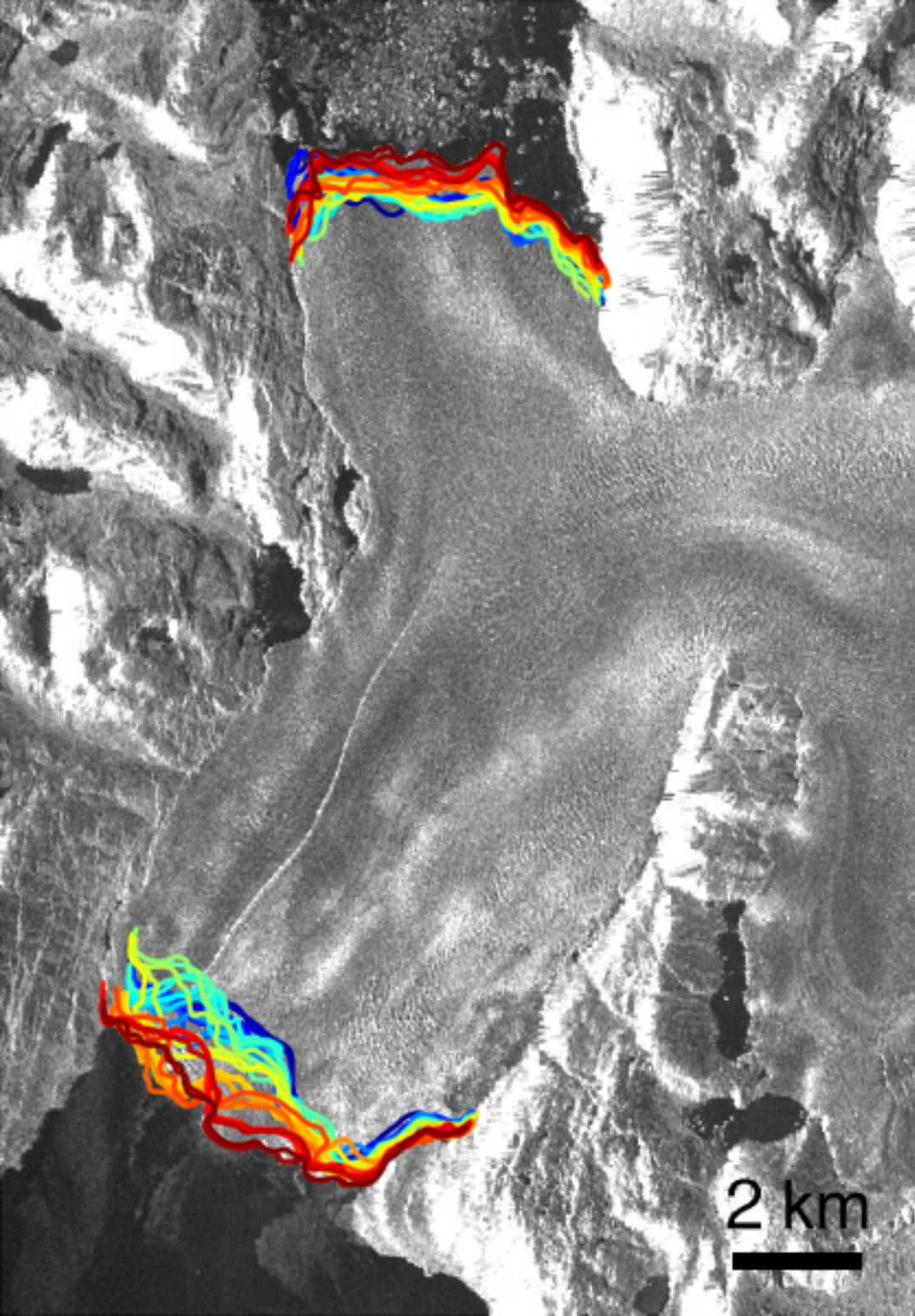


(d)

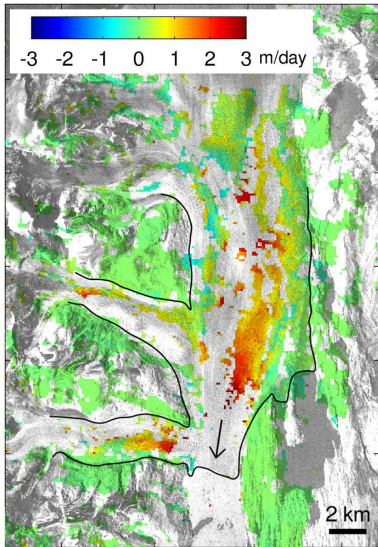


(c)

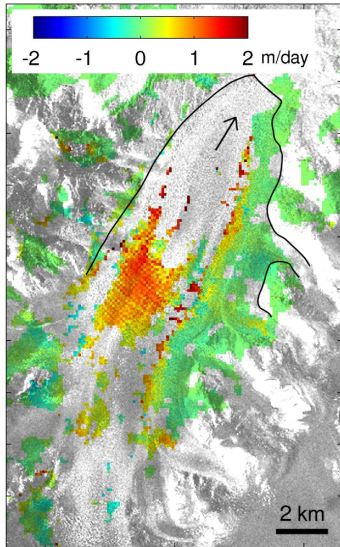




(a)



(b)



(c)

